ARTICLE

doi:10.1038/nature12776

Astrocytes mediate synapse elimination through MEGF10 and MERTK pathways

Won-Suk Chung[1], Laura E. Clarke[1]*, Gordon X. Wang[2]*, Benjamin K. Stafford[3], Alexander Sher[4], Chandrani Chakraborty[1], Julia Joung[1], Lynette C. Foo[5], Andrew Thompson[6], Chinfei Chen[6], Stephen J. Smith[2] & Ben A. Barres[1]

To achieve its precise neural connectivity, the developing mammalian nervous system undergoes extensive activity-dependent synapse remodelling. Recently, microglial cells have been shown to be responsible for a portion of synaptic pruning, but the remaining mechanisms remain unknown. Here we report a new role for astrocytes in actively engulfing central nervous system synapses. This process helps to mediate synapse elimination, requires the MEGF10 and MERTK phagocytic pathways, and is strongly dependent on neuronal activity. Developing mice deficient in both astrocyte pathways fail to refine their retinogeniculate connections normally and retain excess functional synapses. Finally, we show that in the adult mouse brain, astrocytes continuously engulf both excitatory and inhibitory synapses. These studies reveal a novel role for astrocytes in mediating synapse elimination in the developing and adult brain, identify MEGF10 and MERTK as critical proteins in the synapse remodelling underlying neural circuit refinement, and have important implications for understanding learning and memory as well as neurological disease processes.

Astrocytes constitute at least one-third of human brain cells, yet we do not completely understand their function[1]. To understand their functions better, we previously performed gene expression analysis on purified mouse astrocytes and found that they are enriched in genes for phagocytic pathways[2], including two phagocytic receptors, *Megf10* and *Mertk*. MEGF10 is an orthologue of *Drosophila* Draper[3,4] and *Caenorhabditis elegans* CED-1 (ref. 5) that help to mediate axon pruning by glia cells in flies and phagocytosis of apoptotic cells in nematodes. MEGF10 has also been shown to mediate phagocytosis *in vitro*[6] and *in vivo*[7], and the function of MEGF10 requires other proteins, such as GULP1 and ABCA1 (refs 6, 8). MERTK is a member of the MER/AXL/TYRO3 receptor kinase family that mediates shedding of the photoreceptor outer segment by retinal pigment epithelial cells[9,10]. MERTK works with the integrin pathway[11] to regulate CrKII/DOCK180/Rac1 modules in controlling rearrangement of the actin cytoskeleton on phagocytosis[12]. Both MEGF10 and MERTK function as engulfment receptors by recognizing 'eat me signals', such as phosphatidylserine, presented in target debris[13,14]. Because astrocytes highly express phagocytic receptors as well as all their other interacting proteins listed above[2], and one astrocyte has been shown to ensheath thousands of synapses, we reasoned that astrocytes mediate synapse elimination within the developing and adult central nervous system (CNS) through the MEGF10 and/or MERTK phagocytic pathways.

Localization of MEGF10 and MERTK to astrocytes

We first investigated whether MEGF10 and MERTK proteins were present in astrocytes *in vivo*. We found that MEGF10 protein was localized to developing astrocytes visualized by *Aldh1l1-EGFP* transgene expression[2] in the postnatal day 5 (P5) dorsal lateral geniculate nucleus (dLGN) (Fig. 1a). Staining for β-galactosidase driven by the endogenous *Megf10* locus in *Megf10*$^{-/-}$ alleles confirmed specific expression by astrocytes (Fig. 1b). MERTK protein expression was highly localized to developing astrocytes in the P5 dLGN (Fig. 1c), as well as to microglia and endothelial cells (Extended Data Fig. 1). Functional MEGF10 and MERTK proteins were absent in the *Megf10*$^{-/-}$ and *Mertk*$^{-/-}$ postnatal brains (Fig. 1f), confirming the specificity of antibodies. Both *Megf10* and *Mertk* messenger RNA expression and immunoreactivity persisted in adult astrocytes (data not shown and Extended Data Fig. 2).

Astrocytes phagocytose synapses *in vitro* and *in vivo*

We next investigated whether astrocytes could phagocytose synapses and neural debris *in vitro*. Using purified astrocytes with the immunopanning method[15], we developed an *in vitro* engulfment assay, where we cultured astrocytes in the presence of synaptosomes, which are isolated nerve terminals, and found that astrocytes efficiently engulfed synaptosomes (Fig. 1d and Supplementary Video 1). To determine whether these engulfed synaptosomes were targeted to lysosomes, we conjugated the synaptosomes with a pH-sensitive dye, pHrodo, and found that pHrodo-conjugated synaptosomes were efficiently engulfed by astrocytes where they produced bright-red fluorescence (Fig. 1e). The engulfment ability of astrocytes was highly dependent on the presence of secreted factors, as addition of astrocyte-conditioned media (ACM), 5% serum or protein S (a bridging molecule that bridges phosphatidylserine–MERTK interaction)[9] greatly increased the amount of synaptosomes engulfed by astrocytes, whereas addition of fresh media (unconditioned astrocyte growth media, AGM) did not (Fig. 1g). These findings indicate that astrocytes have strong phagocytic capacity that is regulated by secreted, extracellular molecules.

Next, we purified astrocytes from the *Megf10*$^{-/-}$ and *Mertk*$^{-/-}$ postnatal cerebral cortex and performed the *in vitro* engulfment assay. Using image (Fig. 1h) and fluorescence-activated cell sorting (FACS) (Extended Data Fig. 3a, c, e) analysis, we found that *Megf10*$^{-/-}$ and *Mertk*$^{-/-}$ astrocytes each displayed about 50% reduction in their relative engulfment ability. We also compared the phagocytic capacity of enriched microglial populations using FACS analysis, and found

[1]Department of Neurobiology, Stanford University, School of Medicine, Stanford, California 94305, USA. [2]Department of Molecular and Cellular Physiology, Stanford University, School of Medicine, Stanford, California 94305, USA. [3]Department of Ophthalmology and Visual Sciences, University of Michigan, Ann Arbor, Michigan 48105, USA. [4]Santa Cruz Institute of Particle Physic and Department of Physics, University of California, Santa Cruz, California 95064, USA. [5]Institute of Molecular and Cell Biology, A *Star, 61 Biopolis Drive, Proteos Building, 138673 Singapore. [6]Children's Hospital, Harvard Medical School, 300 Longwood Avenue, CLS12250, Boston, Massachusetts 02115, USA.
*These authors contributed equally to this work.

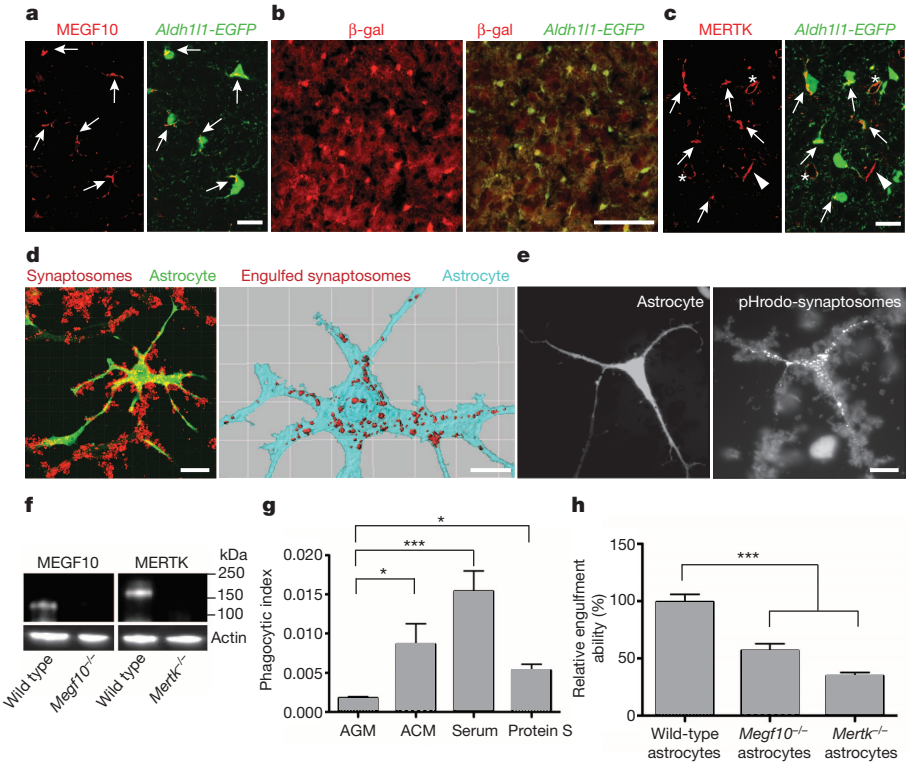

Figure 1 | Localization of MEGF10 and MERTK to astrocytes and their phagocytic roles in purified astrocytes. **a**, Confocal images showing specific MEGF10 (red) localization to astrocytes (green, arrows). **b**, β-gal (red) expression driven by endogenous *Megf10* locus in astrocytes (green). **c**, Confocal images showing MERTK (red) localization to astrocytes (green, arrows) as well as microglia (arrowheads) and endothelial cells (asterisks). **d**, Three-dimensional surface rendering before (left) or after (right) subtracting synaptosomes (red) outside of the astrocytic volume (cyan). **e**, pHrodo-conjugated synaptosomes (right) engulfed by astrocytes (left). **f**, Western blotting showing the absence of functional MEGF10 and MERTK proteins in the brains of P5 $Megf10^{-/-}$ and $Mertk^{-/-}$ mice, respectively. **g**, Compared to AGM, addition of ACM, 5% serum or protein S significantly increased the phagocytic index of astrocytes. **h**, Purified $Megf10^{-/-}$ and $Mertk^{-/-}$ astrocytes showed a 42% and 64% reduction in the engulfment ability, respectively. Representative data from three independent experiments are shown (**g**, **h**). $*P < 0.05$, $***P < 0.001$, one-way ANOVA. Error bars indicate s.e.m. Scale bar: 20 μm (**a**, **c**, **d** (left), **e**); 100 μm (**b**); 10 μm (**d** (right)).

that unlike $Megf10^{-/-}$ microglia (Extended Data Fig. 3b, f), $Mertk^{-/-}$ microglia exhibited a 25% reduction in the relative engulfment ability (Extended Data Fig. 3d, f). Thus, MEGF10 and MERTK are each required for astrocyte-mediated phagocytosis.

To find out whether astrocytes, and their MEGF10 and MERTK pathways, mediate developmental synapse elimination *in vivo*, we took advantage of the retinogeniculate system, a classical model of developmental synapse elimination[16,17]. Initially, axonal projections from retinal ganglion cells (RGCs) form excessive synapses with neurons in the dLGN. During the first week of postnatal development, projections from the contra- and ipsilateral eyes are segregated in the dLGN, so that a single LGN neuron receives RGC inputs from only one eye. Subsequently, all but one or two RGC inputs onto each LGN neuron are removed and the remaining RGC inputs are stabilized. Both of these synapse refinement processes are dependent on spontaneous retinal wave activity[17,18], although how neural activity promotes elimination of synapses is not well understood.

To visualize synapse elimination, RGC projections and their presynaptic compartments were labelled by injecting Alexa594- and Alexa647-conjugated CTB (CTB-594 and CTB-647) into the contra- and ipsilateral eyes of *Aldh1l1-EGFP* transgenic mice at P4, respectively (Fig. 2a). The dLGNs were subsequently imaged at P6 using confocal microscopy (Fig. 2b). Notably, we found a significant amount of CTB-labelled neural debris inside of EGFP-expressing astrocytes (Fig. 2c). Most of the CTB-labelled neural debris engulfed by astrocytes co-localized with LAMP2, a specific marker for late endosome/lysosomes (Fig. 2d)[19], indicating that they are in the process of active degradation.

To find out whether the neural debris engulfed by astrocytes contained synaptic material, first, we used confocal and structured illumination microscopy to examine the P5 dLGN. We found that antibodies to specific presynaptic proteins, including synaptophysin and VGlut2 (Extended Data Fig. 4), whose mRNAs are not expressed at all by astrocytes[2], labelled puncta present within astrocytes. Using array tomography (AT), a super-resolution imaging technique visualizing synaptic protein expression with sub-100-nm volumetric resolution[20], we found that astrocytes engulfed much of the CTB-labelled debris as well as synaptic material immunolabelled for both presynaptic (Bassoon) and postsynaptic (PSD-95 and GluR1) proteins (Extended Data Fig. 5). Moreover, putative synapses that contained both CTB-positive presynaptic, and PSD-95-positive (Fig. 2e) or GluR1-positive (Fig. 2f) postsynaptic proteins were frequently found adjoined together inside of astrocytes, indicating that entire synapses had been engulfed. To examine cellular details of the engulfed synapses by astrocytes, the P5 dLGN was also imaged with serial block-face scanning electron microscopy (SBEM, Fig. 2g–j). We found many incidents showing double-membrane-bound inclusions with vesicles that are the same size as the presynaptic vesicles (Fig. 2g–j) being completely surrounded by astrocytic cytoplasm identified by the presence of glycogen granules (Fig. 2j and Supplementary Video 2)[21]. The inner membrane of the engulfed presynaptic material within astrocytes displayed irregular morphology (Fig. 2h, i), suggesting that the material was in the process of active degradation. Some of the inclusion seems to be in the further process of degradation as it was found in structures with the characteristics of lysosomal bodies[21] (Fig. 2h–j). These data indicate that astrocytes actively engulf synapses and suggest that astrocytes are actively helping to mediate retinogeniculate refinement.

We next developed an image-processing algorithm that allowed us to visualize only the engulfed puncta inside of astrocytes (Fig. 3a). By measuring the phagocytic index at different time points, we found that the highest amount of astrocyte-mediated phagocytosis occurs at the peak period of eye-specific segregation before P6 (Fig. 3d), indicating that there is a critical developmental time window for synapse elimination by astrocytes.

To determine whether MEGF10 and MERTK are required for astrocyte-mediated synapse elimination, we next measured the phagocytic index of astrocytes in the $Megf10^{-/-}$ and $Mertk^{-/-}$ dLGNs (Fig. 3b, c). As we had observed *in vitro*, we found that astrocytes *in vivo* in the $Megf10^{-/-}$ and $Mertk^{-/-}$ dLGNs displayed a 45% and 58% reduction, respectively, in their relative engulfment ability compared to wild type (Fig. 3e). Furthermore, astrocytes in the $Megf10^{-/-}$; $Mertk^{-/-}$ dLGNs showed a further decrease in their relative engulfment ability of about 85% (Fig. 3e), indicating that MEGF10 and MERTK work in parallel to mediate synapse elimination in developing brains.

Recently, it has been shown that microglial cells also mediate synapse elimination in the developing retinogeniculate system[22]. To investigate the relative contributions of microglia and astrocytes in

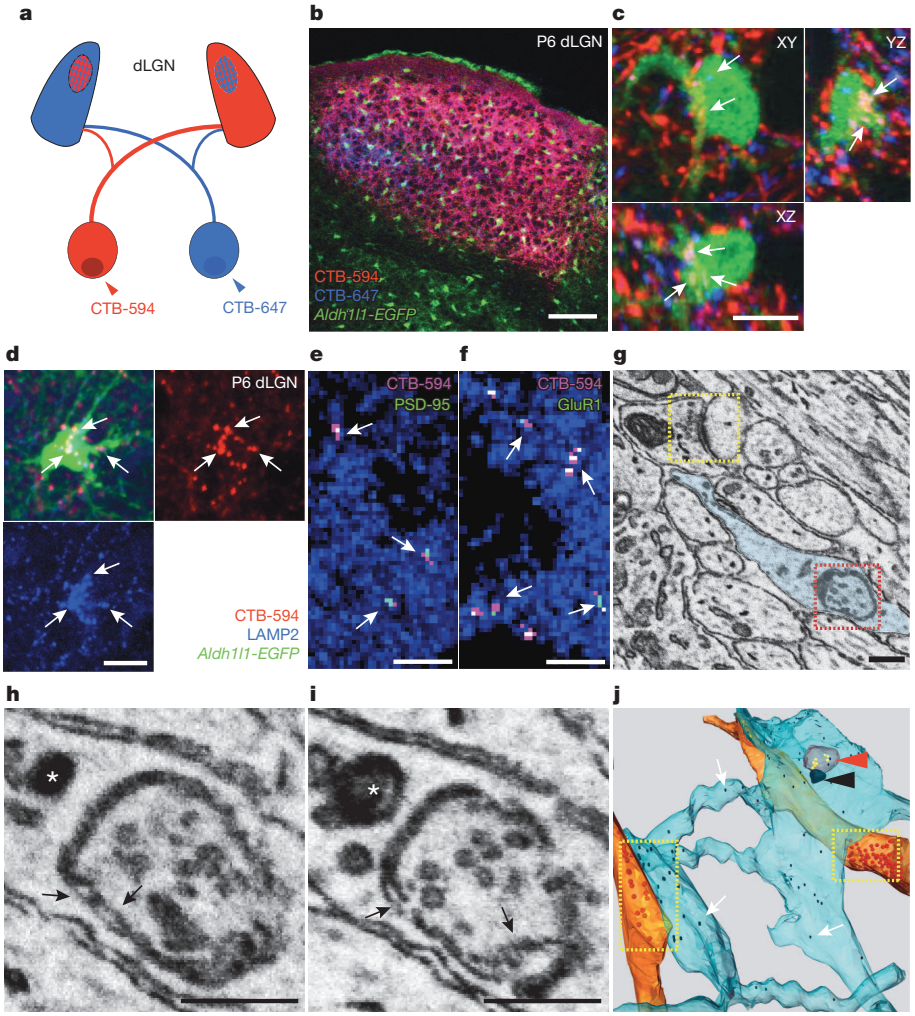

Figure 2 | Astrocytes mediate synapse elimination in the developing dLGN. **a**, Schematic diagram of anterograde RGC labelling with CTB-594 (red) and CTB-647 (blue), projecting to the developing dLGN. **b**, Contralateral (red) and ipsilateral (blue) projections in the P6 dLGN from *Aldh1l1-EGFP* (green) transgenic animals. Scale bar: 100 μm. **c**, Confocal optical sections through *xy*, *xz* and *yz* axes showing CTB-labelled debris (arrows) inside astrocytes (green). Scale bar: 10 μm. **d**, 3D-max projection showing that CTB-labelled debris (red, arrows) engulfed by astrocytes (green) was co-localized with LAMP2-positive lysosomes (blue). Scale bar: 10 μm. **e**, **f**, 3D-max projection AT images showing engulfed putative synapses (arrows) in astrocytes (blue). Engulfed putative synapses are defined as EYFP (blue) enveloped CTB-594 (magenta) and PSD-95 (**e**) or GluR1 (**f**) (green) that are within 200 nm of each other. Scale bar: 5 μm. **g**, Low-magnification SBEM micrograph showing an intact synapse (yellow rectangle; note the presynaptic vesicles and postsynaptic density) and astrocytic process (cyan) containing engulfed presynaptic material (red rectangle; note the vesicles that are the same size as the presynaptic vesicles). **h**, **i**, Consecutive high-magnification SBEM micrographs showing the engulfed presynaptic structure with irregular double-membrane morphology (arrows) and second inclusion (asterisks). **j**, Three-dimensional reconstruction of SBEM micrographs confirmed that astrocytic processes (cyan) with glycogen granules (arrows) fully engulfed presynaptic material (red arrowhead) as well as the second inclusion (black arrowhead). Synaptic vesicles in the intact synapse (yellow rectangles), in the axons (orange) and the engulfed presynaptic material are shown in red and yellow spheres, respectively. Scale bar: 0.4 μm (**g**, **h**, **i**).

synapse elimination, we measured the phagocytic indices of astrocytes and microglia together during P3–P9. Only during P3–P6, microglia engulfed more CTB-labelled debris than astrocytes per unit cell volume (Extended Data Fig. 6c). However, we found that astrocytes significantly outnumbered microglia by 10-, 7-, 6- and 4-fold at P5, P6, P7 and P9, respectively (Extended Data Fig. 6a, b). As a result, the total amount of engulfed CTB-labelled debris in a given imaging field was much greater in astrocytes (Extended Data Fig. 6d) during P3–P9, indicating that the total amount of synaptic pruning by astrocytes could exceed that by microglia in the developing LGN.

It is important to note that MERTK protein is localized to astrocytes as well as to microglia (Fig. 1c and Extended Data Fig. 1). Therefore, to determine whether MERTK contributes to the phagocytic function of microglia in the developing dLGN, we examined the phagocytic index of microglia in the *Mertk*$^{-/-}$ dLGN during P3–P6. Unexpectedly, we found that the *Mertk*$^{-/-}$ microglia displayed a transient increase in the amount of engulfed CTB-labelled debris compared to wild type only during P4–P5 (Extended Data Fig. 7). Thus, our *in vivo* data indicate that MERTK is dispensable for the phagocytic function of microglia in the developing dLGN, and that microglia can compensate to some extent for reduced astrocyte-mediated phagocytosis of synapses.

Neural circuit pruning and refinement by astrocytes

What is the role of astrocyte-mediated phagocytosis of synapses? Astrocytes could be removing axonal and synaptic debris produced from already retracting pre- and postsynaptic compartments that are no longer functional. Alternatively, astrocytes could actively promote synapse disassembly and clearance of unwanted synapses, leaving strong inputs intact for further stabilization. To address this issue, we labelled contra- and ipsilateral projections with CTB-594 and CTB-488, respectively, at P29 and examined the dLGN at P30 when eye-specific segregation is fully accomplished. We found that in *Megf10*$^{-/-}$; *Mertk*$^{-/-}$ mice, eye-specific segregation failed to occur properly (Fig. 3f, g). The overlap between contra- and ipsilateral projections was significantly increased compared to wild-type and single-knockout mice, indicating incomplete segregation (Fig. 3g). Consistent with this finding, the area of dLGN occupied by ipsilateral projections was significantly increased in *Megf10*$^{-/-}$; *Mertk*$^{-/-}$ mice (Fig. 3h). Because photoreceptors in the *Mertk*$^{-/-}$ retina show progressive degeneration starting from P25 (refs 9, 10), we examined spontaneous retinal waves that drive eye-specific segregation and found that they were intact in the P6 *Megf10*$^{-/-}$; *Mertk*$^{-/-}$ retina (Extended Data Fig. 8), indicating that incomplete eye-specific segregation was not due to any retinal defects.

To measure directly whether the number of functional retinogeniculate synapses is increased in *Megf10*$^{-/-}$; *Mertk*$^{-/-}$ mice, we performed electrophysiology with acute brain slices of P15–18 mice. Figure 4a, b shows the excitatory postsynaptic currents (EPSCs) from dLGN neurons of wild-type and *Megf10*$^{-/-}$; *Mertk*$^{-/-}$ littermates, respectively, in response to incremental increases in optic tract stimulation. The visually discernible 'steps' in the current traces were counted and compared between wild-type and *Megf10*$^{-/-}$; *Mertk*$^{-/-}$ neurons (Fig. 4c). As previously reported[18,23], we found that by P18 most (91%) of wild-type neurons were innervated by between 1–4 inputs. In contrast, *Megf10*$^{-/-}$; *Mertk*$^{-/-}$ neurons received a larger number of

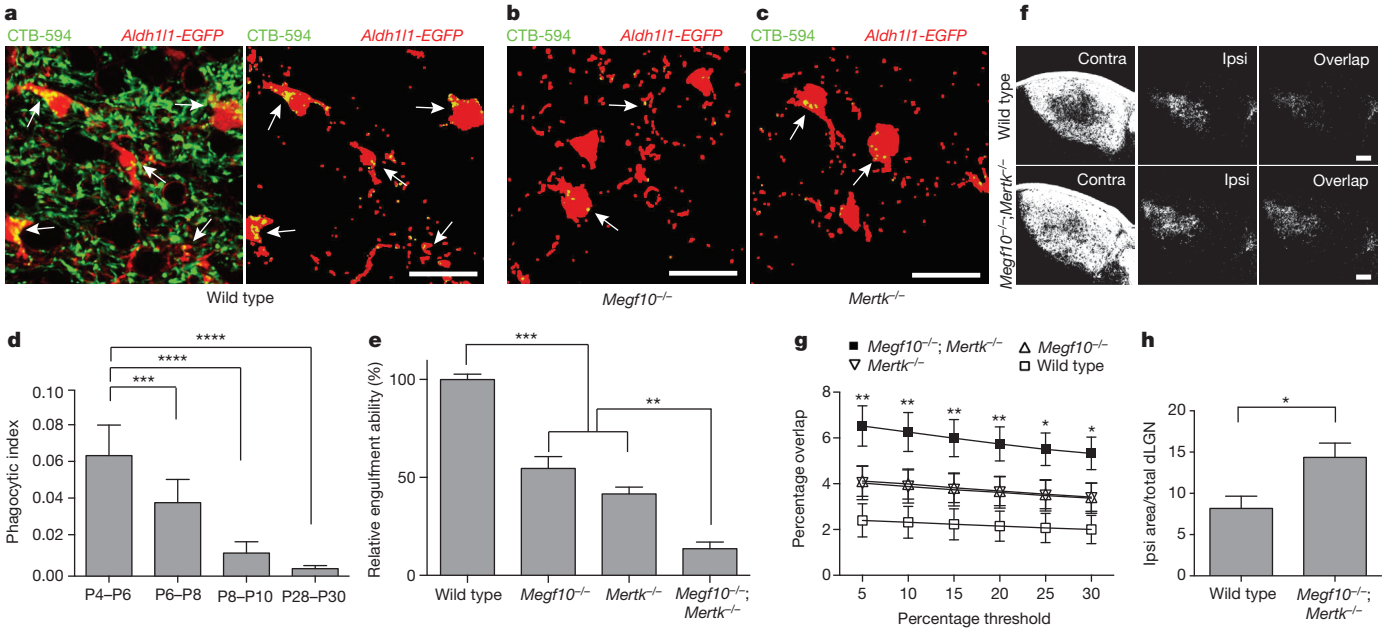

Figure 3 | Astrocytes mediate developmental synapse pruning and remodelling through MEGF10 and MERTK pathways. **a**, Confocal images of the wild-type P6 dLGN before and after subtracting CTB-594 (pseudo-coloured green) outside of astrocytes (pseudo-coloured red). **b**, **c**, In *Megf10*$^{-/-}$ (**b**) and *Mertk*$^{-/-}$ (**c**) mice, the amount of engulfed CTB-594 (green) by astrocytes (red) was significantly reduced (arrows). **d**, The highest astrocyte-mediated phagocytosis occurs during P4–P6. $n = 3$ mice per age. **e**, *Megf10*$^{-/-}$ and *Mertk*$^{-/-}$ mice showed significantly reduced astrocyte-mediated phagocytosis (45% and 58% reduction, respectively), which was further reduced in *Megf10*$^{-/-}$; *Mertk*$^{-/-}$ mice (85% reduction). $n = 4$ mice per group. **f**, **g**, Overlap between contra- and ipsilateral projections was significantly increased in *Megf10*$^{-/-}$; *Mertk*$^{-/-}$ mice at P30 (**f**), independently from the threshold value used in the analysis (**g**). $n = 4$ mice per group. **h**, The area of dLGN occupied by ipsilateral projections was significantly increased in P30 *Megf10*$^{-/-}$; *Mertk*$^{-/-}$ mice. $n = 4$ mice per group. $^{*}P < 0.05$, $^{**}P < 0.01$, $^{***}P < 0.001$, $^{****}P < 0.0001$, one-way ANOVA for all except **h** (*t*-test). NS, not significant. Error bars indicate s.e.m. Scale bar: 20 μm (**a**–**c**); 100 μm (**f**).

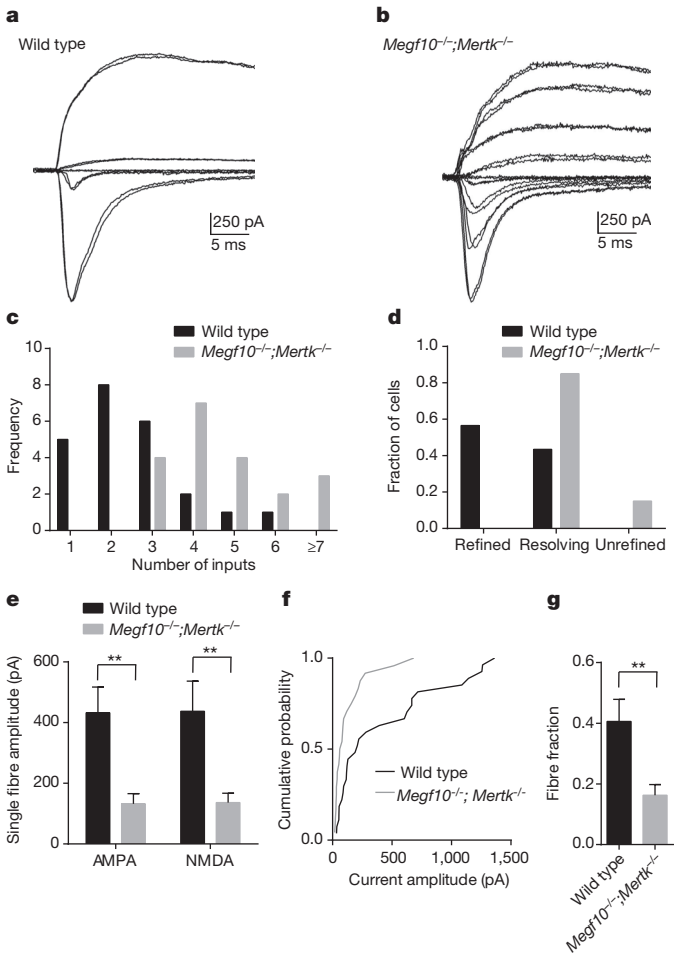

inputs, as shown by a rightward shift in the distribution of the number of inputs (Fig. 4c). As a result, wild-type neurons fell into either the refined or the resolving category (Fig. 4d), whereas we found no fully refined *Megf10*$^{-/-}$; *Mertk*$^{-/-}$ neurons at this age, and most *Megf10*$^{-/-}$; *Mertk*$^{-/-}$ neurons remained multiply innervated (Fig. 4d), indicating a significant deficit in synapse elimination.

Next, we used minimal stimulation to measure the synaptic properties of individual fibres. We found that the mean amplitude of AMPA (α-amino-3-hydroxy-5-methyl-4-isoxazole propionic acid) and NMDA (*N*-methyl-D-aspartate) single-fibre responses were significantly reduced in *Megf10*$^{-/-}$; *Mertk*$^{-/-}$ neurons (Fig. 4e) with a leftward shift in a cumulative distribution plot compared to wild-type neurons (Fig. 4f). We also compared the fibre fraction ratios by quantifying the contribution of each single fibre EPSC to the maximal evoked response and found that the fibre fraction ratio was significantly reduced in *Megf10*$^{-/-}$; *Mertk*$^{-/-}$ neurons (Fig. 4g), with each fibre contributing only 16.3 ± 0.03% of the total innervation compared to 40.6 ± 0.07% in wild-type cells. Taken together, these data indicate that these neurons are innervated by a greater number of

Figure 4 | dLGN neurons are abnormally innervated by multiple weak inputs in *Megf10*$^{-/-}$; *Mertk*$^{-/-}$ mice. **a**, **b**, Representative traces of superimposed EPSCs evoked by increasing intensities of optic tract stimulation recorded from individual wild-type (**a**) and *Megf10*$^{-/-}$; *Mertk*$^{-/-}$ (**b**) dLGN neurons at P15–18. **c**, *Megf10*$^{-/-}$; *Mertk*$^{-/-}$ neurons receive a significantly larger number of inputs ($P = 0.003$). **d**, Most *Megf10*$^{-/-}$; *Mertk*$^{-/-}$ neurons were in the resolving or unrefined category, whereas most wild-type neurons were in the refined category. **e**, *Megf10*$^{-/-}$; *Mertk*$^{-/-}$ neurons had significantly smaller AMPA ($P = 0.002$) and NMDA ($P = 0.008$) single-fibre currents. **f**, *Megf10*$^{-/-}$; *Mertk*$^{-/-}$ neurons had significantly more small-amplitude single-fibre AMPA current responses in cumulative probability histograms ($P = 0.023$). **g**, *Megf10*$^{-/-}$; *Mertk*$^{-/-}$ neurons had a significantly reduced mean fibre fraction ($P = 0.005$). Recordings were obtained from 23 wild-type cells and 20 *Megf10*$^{-/-}$; *Mertk*$^{-/-}$ cells. $^{**}P < 0.01$, *t*-test except **c** and **f** (Kolmogorov–Smirnov test). Error bars indicate s.e.m.

weak inputs and demonstrate that astrocytes contribute to normal neural circuit pruning and refinement in the developing CNS by phagocytosing weak synapses through MEGF10 and MERTK pathways.

Neural activity promotes synapse pruning by astrocytes

Retinogeniculate segregation does not occur when retinal wave activity is blocked[17,24], raising the question of whether neural activity has a role in astrocyte-mediated synapse elimination. To find out, we intraocularly injected epibatidine, a potent agonist for neuronal nicotinic acetylcholine receptors, to block specifically the spontaneous retinal waves[17,25,26]. Previous work has shown that injecting epibatidine binocularly blocks eye-specific segregation in dLGN, whereas injecting epibatidine monocularly preserves eye-specific segregation, inducing the affected weaker projections to lose their territory preferentially. When we injected epibatidine binocularly, the total amount of both engulfed contra- (CTB-594) and ipsilateral (CTB-647) projections by astrocytes was significantly reduced (Fig. 5a, b, d), whereas the ratio of engulfed contra- versus ipsilateral projections was unchanged compared to control injections (Fig. 5e). Notably, when epibatidine was injected monocularly to the contralateral eye of the wild-type mice, astrocytes engulfed the weaker projections preferentially (Fig. 5c, d), significantly increasing the ratio of engulfed contra- versus ipsilateral projections by astrocytes (Fig. 5e). This preferential engulfment of weaker projections was significantly reduced in the *Megf10*$^{-/-}$ and *Mertk*$^{-/-}$ background (Fig. 5d, e). These data show that retinal activity strongly promotes synapse elimination by enhancing the amount of astrocyte-mediated phagocytosis via the MEGF10 and MERTK pathways in the dLGN.

Synapse elimination by astrocytes in adult brains

Synapses in the adult brain, especially dendritic spines, are dynamic structures that turn over rapidly during activity-dependent synaptic plasticity induced by learning and memory[27–29]. Because MEGF10 and MERTK are highly localized to astrocytes in the adult CNS and not just the developing CNS (Extended Data Fig. 2), we next asked whether synapse engulfment and elimination by astrocytes persists in the adult CNS. By using AT, we analysed EYFP-expressing astrocytes in the 1- and 4-month-old somatosensory cortex by immunostaining with astrocyte- and synapse-specific antibodies (Extended Data Fig. 9). Three-dimensional (3D)-max projection AT images revealed that both putative excitatory (puncta containing Bassoon and PSD-95) and inhibitory (puncta containing Gephyrin and VGAT) synapses were robustly engulfed by astrocytes throughout the 1- and 4-month-old cortex (Fig. 6a–c). Notably, we found that more excitatory synapses were engulfed by 1-month-old than 4-month-old cortical astrocytes (Fig. 6d), probably due to a higher rate of developmental synapse pruning of excitatory projections in the younger brains[30]. In contrast, engulfed putative inhibitory synapses showed about the same density within 1- and 4-month-old cortical astrocytes (Fig. 6d). These data show that engulfment of both excitatory and inhibitory synapses by astrocytes continues in the adult CNS.

Concluding remarks

Our findings demonstrate that astrocytes actively contribute to the activity-dependent synapse elimination that mediates neural circuit refinement in the developing CNS by phagocytosing synapses via the MEGF10 and MERTK pathways, and that astrocytes continue to engulf synapses in the adult CNS. These findings reveal a previously unknown role for astrocytes, provide new information about the mechanisms underlying neural circuit refinement during development, and add to the growing evidence that substantial synapse turnover and remodelling occurs in the adult CNS. Astrocytes thus share with microglia the ability to actively engulf and eliminate synapses in response to neural activity, but synapse engulfment by astrocytes is independent of complement protein C1q (ref. 31 and data not shown), and uses distinct phagocytic pathways from microglia. Astrocytes in *Drosophila* also phagocytose synapses, indicating that the phagocytic function of astrocytes is evolutionarily conserved[32]. These findings have important implications and raise many questions. How does neural activity control the rate of astrocyte-mediated synapse phagocytosis, do astrocytes and microglia phagocytose different synapse types or circuits, and how do astrocytes decide which synapses to engulf? Because MEGF10 and MERTK phagocytic receptors initiate the engulfment process by recognizing phosphatidylserine presented by target debris, an important question is whether the weak synapses that need to be eliminated present 'eat me signals' locally and if so what their identities are. Most notably, our findings suggest that the activity-dependent engulfment of synapses by astrocytes has an active role in

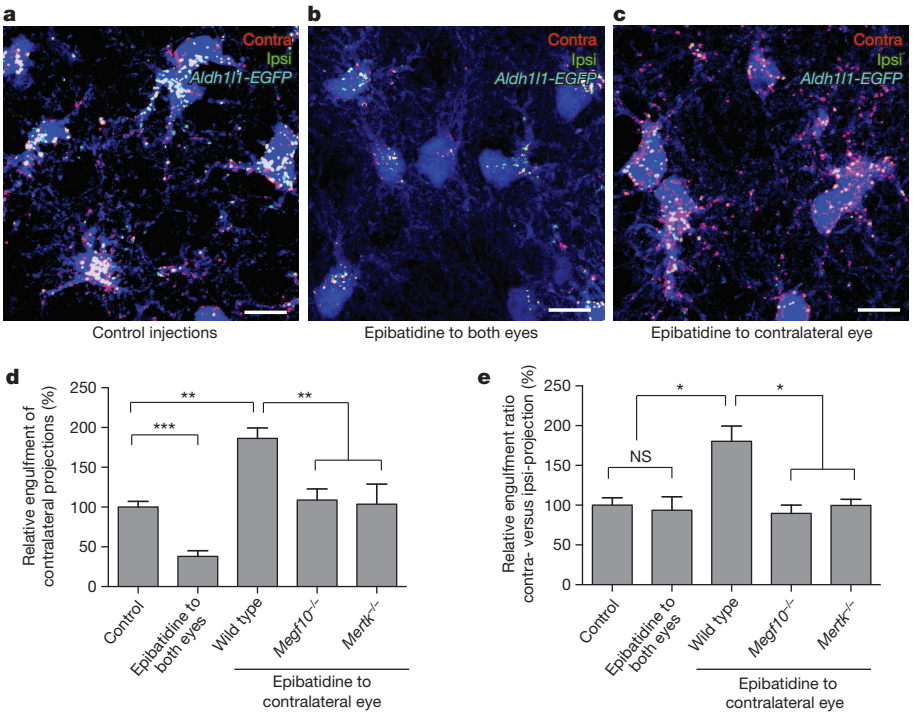

Figure 5 | Neural activity promotes astrocyte-mediated synapse elimination through MEGF10 and MERTK. **a**–**c**, 3D-max projection confocal images showing CTB-594-labelled contralateral (red) and CTB-647-labelled ipsilateral (green) debris engulfed by astrocytes (blue) in P6 dLGN, comparing control (**a**), binocular (**b**) and monocular (**c**) injections. Red and green debris co-localized in astrocytes (blue) appears as bright yellow. **d**, Relative engulfment of contralateral projections by astrocytes was significantly reduced after binocular epibatidine injections whereas it was significantly increased after monocular epibatidine injections to the wide-type contralateral eye. However, this increased engulfment was reduced in the *Megf10*$^{-/-}$ or *Mertk*$^{-/-}$ background. **e**, In binocular epibatidine injection cases, the ratio of engulfed contralateral versus ipsilateral projections by astrocytes was unchanged compared to control injections whereas it was significantly increased after monocular epibatidine injections to wild-type contralateral eye. However, this increased ratio of engulfed contralateral versus ipsilateral projections was reduced in the *Megf10*$^{-/-}$ or *Mertk*$^{-/-}$ background. $n = 4$ mice per treatment. $^{*}P < 0.05$, $^{**}P < 0.01$, $^{***}P < 0.001$, one-way ANOVA. NS, not significant. Error bars indicate s.e.m. Scale bar: 10 μm (**a**–**c**).

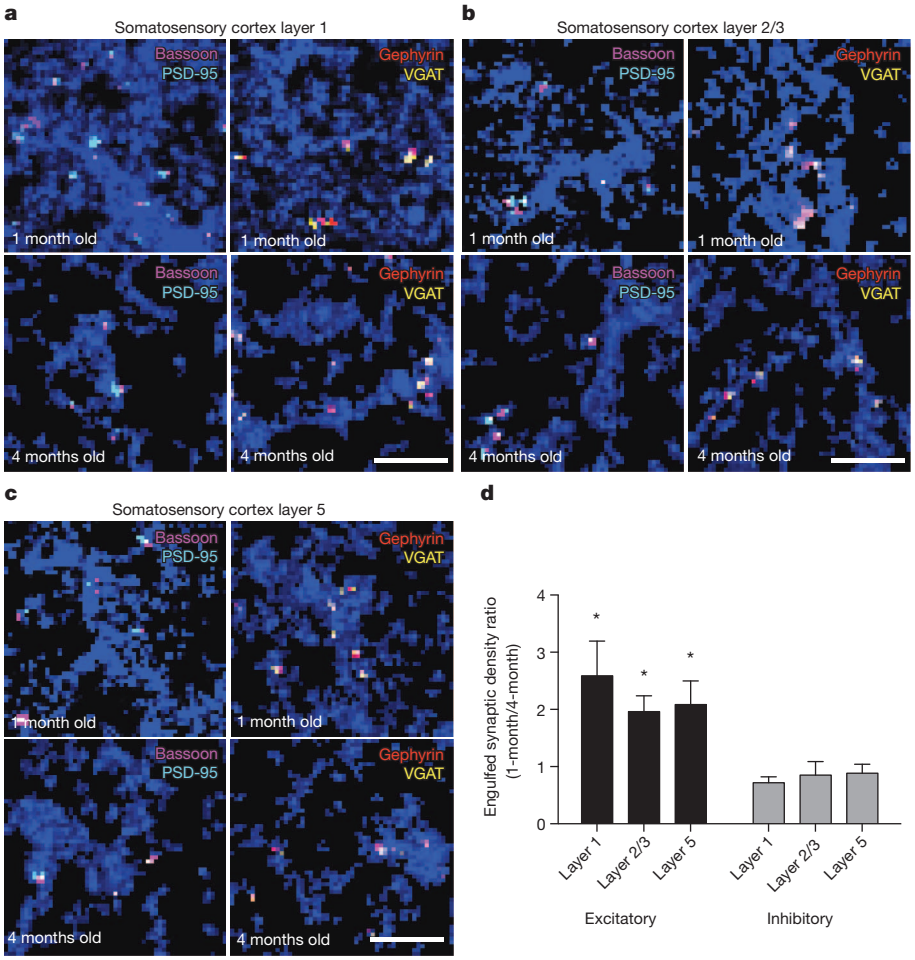

Figure 6 | Astrocytes in the adult cortex continuously engulf synapses. **a**–**c**, 3D-max projection AT images showing EYFP-labelled cortical astrocytes (blue) and engulfed putative excitatory synapses (Bassoon, magenta, and PSD-95, cyan) and inhibitory synapses (VGAT, yellow, and Gephyrin, red) from layers 1 (**a**), 2/3 (**b**) and 5 (**c**) of the 1- and 4-month-old mouse somatosensory cortex (total volume = 60 μm by 60 μm by 2.8 μm). Engulfed synapses were defined as EYFP (blue) enveloped presynaptic and postsynaptic puncta that were within 200 nm of each other. Scale bar: 2.5 μm. **d**, The density ratio of engulfed excitatory and inhibitory synapses by astrocytes between the 1-month-old and 4-month-old cortex. $n = 3$ mice per age. $^*P < 0.05$, *t*-test. Error bars indicate s.e.m.

continually remodelling the synaptic architecture of our brains. Whether such remodelling underlies learning and memory, and whether a declining rate of synapse engulfment by astrocytes throughout life could contribute to critical period plasticity during development or to synaptic senescence and neurodegeneration with ageing, are important questions for future study.

METHODS SUMMARY

All procedures were conducted in accordance with the animal care standards set forth by the National Institutes of Health and approved by Stanford University's Administrative Panel on Laboratory Animal Care. Astrocytes and microglial cells were purified from P4–P6 mouse cortex and cultured in serum-free conditions. All experiments with mutants were performed blindly without knowledge of their genotype.

Online Content Any additional Methods, Extended Data display items and Source Data are available in the online version of the paper; references unique to these sections appear only in the online paper.

Received 11 March; accepted 11 October 2013.
Published online 24 November 2013.

1. Barres, B. A. The mystery and magic of glia: a perspective on their roles in health and disease. *Neuron* **60,** 430–440 (2008).
2. Cahoy, J. D. *et al.* A transcriptome database for astrocytes, neurons, and oligodendrocytes: a new resource for understanding brain development and function. *J. Neurosci.* **28,** 264–278 (2008).
3. Ziegenfuss, J. S. *et al.* Draper-dependent glial phagocytic activity is mediated by Src and Syk family kinase signalling. *Nature* **453,** 935–939 (2008).
4. MacDonald, J. M. *et al.* The *Drosophila* cell corpse engulfment receptor Draper mediates glial clearance of severed axons. *Neuron* **50,** 869–881 (2006).
5. Zhou, Z., Hartwieg, E. & Horvitz, H. R. CED-1 is a transmembrane receptor that mediates cell corpse engulfment in *C. elegans*. *Cell* **104,** 43–56 (2001).
6. Hamon, Y. *et al.* Cooperation between engulfment receptors: the case of ABCA1 and MEGF10. *PLoS ONE* **1,** e120 (2006).
7. Wu, H. H. *et al.* Glial precursors clear sensory neuron corpses during development via Jedi-1, an engulfment receptor. *Nature Neurosci.* **12,** 1534–1541 (2009).
8. Kinchen, J. M. *et al.* Two pathways converge at CED-10 to mediate actin rearrangement and corpse removal in *C. elegans*. *Nature* **434,** 93–99 (2005).
9. Prasad, D. *et al.* TAM receptor function in the retinal pigment epithelium. *Mol. Cell. Neurosci.* **33,** 96–108 (2006).
10. Duncan, J. L. *et al.* An RCS-like retinal dystrophy phenotype in mer knockout mice. *Invest. Ophthalmol. Vis. Sci.* **44,** 826–838 (2003).
11. Finnemann, S. C. Focal adhesion kinase signaling promotes phagocytosis of integrin-bound photoreceptors. *EMBO J.* **22,** 4143–4154 (2003).
12. Wu, Y., Singh, S., Georgescu, M. M. & Birge, R. B. A role for Mer tyrosine kinase in αvβ5 integrin-mediated phagocytosis of apoptotic cells. *J. Cell Sci.* **118,** 539–553 (2005).
13. Tung, T. T. *et al.* Phosphatidylserine recognition and induction of apoptotic cell clearance by *Drosophila* engulfment receptor Draper. *J. Biochem.* **153,** 483–491 (2013).
14. Hochreiter-Hufford, A. & Ravichandran, K. S. Clearing the dead: apoptotic cell sensing, recognition, engulfment, and digestion. *Cold Spring Harb. Perspect. Biol.* **5** (2013).
15. Foo, L. C. *et al.* Development of a method for the purification and culture of rodent astrocytes. *Neuron* **71,** 799–811 (2011).
16. Shatz, C. J. & Sretavan, D. W. Interactions between retinal ganglion cells during the development of the mammalian visual system. *Annu. Rev. Neurosci.* **9,** 171–207 (1986).
17. Penn, A. A., Riquelme, P. A., Feller, M. B. & Shatz, C. J. Competition in retinogeniculate patterning driven by spontaneous activity. *Science* **279,** 2108–2112 (1998).
18. Hooks, B. M. & Chen, C. Distinct roles for spontaneous and visual activity in remodeling of the retinogeniculate synapse. *Neuron* **52,** 281–291 (2006).
19. Cuervo, A. M. & Dice, J. F. A receptor for the selective uptake and degradation of proteins by lysosomes. *Science* **273,** 501–503 (1996).
20. Wang, G. & Smith, S. J. Sub-diffraction limit localization of proteins in volumetric space using Bayesian restoration of fluorescence images from ultrathin specimens. *PLOS Comput. Biol.* **8,** e1002671 (2012).
21. Peters, A., Palay, S. L., Webster, H. & d. *The Fine Structure of the Nervous System: the Neurons and Supporting Cells* (Saunders, 1976).
22. Schafer, D. P. *et al.* Microglia sculpt postnatal neural circuits in an activity and complement-dependent manner. *Neuron* **74,** 691–705 (2012).

23. Chen, C. & Regehr, W. G. Developmental remodeling of the retinogeniculate synapse. *Neuron* **28,** 955–966 (2000).
24. Shatz, C. J. & Stryker, M. P. Prenatal tetrodotoxin infusion blocks segregation of retinogeniculate afferents. *Science* **242,** 87–89 (1988).
25. Stellwagen, D. & Shatz, C. J. An instructive role for retinal waves in the development of retinogeniculate connectivity. *Neuron* **33,** 357–367 (2002).
26. Huberman, A. D., Stellwagen, D. & Chapman, B. Decoupling eye-specific segregation from lamination in the lateral geniculate nucleus. *J. Neurosci.* **22,** 9419–9429 (2002).
27. Xu, T. *et al.* Rapid formation and selective stabilization of synapses for enduring motor memories. *Nature* **462,** 915–919 (2009).
28. Yang, G., Pan, F. & Gan, W. B. Stably maintained dendritic spines are associated with lifelong memories. *Nature* **462,** 920–924 (2009).
29. Roberts, T. F., Tschida, K. A., Klein, M. E. & Mooney, R. Rapid spine stabilization and synaptic enhancement at the onset of behavioural learning. *Nature* **463,** 948–952 (2010).
30. Paolicelli, R. C. *et al.* Synaptic pruning by microglia is necessary for normal brain development. *Science* **333,** 1456–1458 (2011).
31. Stevens, B. *et al.* The classical complement cascade mediates CNS synapse elimination. *Cell* **131,** 1164–1178 (2007).
32. Tasdemir-Yilmaz, O. & Freeman, M. R. Astrocytes engage unique molecular programs to engulf pruned neuronal debris from distinct subsets of neurons. *Genes Dev.* (in the press).

Supplementary Information is available in the online version of the paper.

Acknowledgements We thank D. Vollrath for discussions and MERTK antibody. We also thank H. M. Lee for helping us set up electrophysiology experiments as well as for discussions. Part of the data was acquired at Stanford Neuroscience Microscopy Service (NMS), supported by NIH NS069375. W.-S.C. was supported in part by a postdoctoral fellowship from the Damon Runyon Cancer Research Foundation (DRG 2020-09). L.E.C. was supported in part by an EMBO ALTF fellowship. This work was supported by grants from the NIH (5 R21NS072556, B.A.B.) and a Brain Disorder Award from the Mcknight Foundation to B.A.B. We thank V. and S. Coates for their generous support.

Author Contributions W.-S.C. and B.A.B. designed the experiments and wrote the paper. W.-S.C. performed experiments and analysed data. L.E.C. performed and analysed electrophysiology recordings from LGN neurons with support from A.T. and C. Chen. G.X.W. performed and analysed array tomography experiments. B.K.S. performed and analysed spontaneous retinal wave recording with support from A.S. C. Chakraborty, J.J., L.C.F. and S.J.S. provided technical support.

Author Information Reprints and permissions information is available at www.nature.com/reprints. The authors declare no competing financial interests. Readers are welcome to comment on the online version of the paper. Correspondence and requests for materials should be addressed to W.-S.C. (wschung@stanford.edu).

METHODS

Animals. *Megf10*$^{tm1(KOMP)Vlcg}$ and B6;129-*Mertk*^{tm1Grl}/J (ref. 33) mice were obtained from KOMP and Jackson Laboratories, respectively. *Aldh1l1-EGFP* (ref. 2) and *CX3CR1-EGFP* (ref. 22) transgenic lines were used to visualize astrocytes and microglia, respectively. For array tomography, a reporter line [*Gt(ROSA)26Sor*$^{tm3(CAG-EYFP)Hze}$/J] and *cre* lines [Tg(*GFAP-cre*)25Mes/J for the dLGN and Tg(*Gfap-cre*)77.6Mvs/J for the cortex] from Jackson Laboratories were crossed together to get astrocyte-specific EYFP expression. All lines were maintained by breeding with C57BL/6 mice. All experiments with mutants were performed blindly without knowledge of their genotype.

Immunohistochemistry. Animals were anaesthetized with a ketamine (100 mg kg^{-1})/xylazine (20 mg kg^{-1}) cocktail, and perfused with PBS followed by 4% paraformaldehyde. Brains were dissected out, post-fixed overnight in 4% paraformaldehyde at 4 °C and transferred to 30% sucrose for 24 h. After embedding brain tissues with OCT compound (Tissue-Tek), 10 μm tissue sections were prepared by Leica cryostats. The following antibodies were used: MEGF10 (rabbit polyclonal from Sigma and Millipore), MERTK (goat polyclonal Biotin conjugated from R&D, rabbit polyclonal: gift from D. Vollrath), β-galactosidase (chicken polyclonal from Abcam and Aves Labs), GFP (chicken polyclonal from Aves Labs), LAMP2 (rat monoclonal from Abcam), synaptophysin (mouse monoclonal from Millipore), VGlut2 (guinea-pig polyclonal from Millipore), BSL (biotin-conjugated BSL from Vector Labs), IBA1 (rabbit polyclonal from Wako and mouse monoclonal Millipore), Bassoon (mouse monoclonal from Abcam), PSD-95 (rabbit monoclonal from Cell Signaling Technology), gephyrin (mouse monoclonal from Biosciences Pharmingen) and VGAT (mouse monoclonal from Synaptic Systems). Staining for MEGF10 and MERTK was achieved by using Tyramide Signal Amplification (TSA) system from PerkinElmer. Staining for other antibodies was performed as described previously[31] with appropriate secondary antibodies conjugated with Alexa fluorophore (Invitrogen). Images were acquired using Zeiss LSM510 inverted confocal, Zeiss AxioImager fluorescence microscopy and Applied Precision OMX V4 structured illlumination super-resolution microscopy.

Synaptosome purification. Synaptosomes were purified by percoll gradient from the adult mouse brains as described previously[34]. To obtain red fluorescent synaptosomes, *Gt(ROSA)26Sor*$^{tm9(CAG-tdTomato)Hze}$/J line from Jackson Laboratories was crossed to ubiquitous *cre* line (heat-shock-promoter-driven *cre* line), and the tdTomato-expressing adult brains were used for purifying synaptosomes. To obtain pHrodo-conjugated synaptosomes, synaptosomes purified from the wild-type adult brains were incubated with pHrodo red, succinimidyl ester (Invitrogen) in 0.1 M sodium carbonate (pH 9.0) at room temperature with gentle agitation[35]. After 2-h incubation, unbound pHrodo was washed out by multiple rounds of centrifugation and pHrodo-conjugated synaptosomes were re-suspended with isotonic buffer containing 5% DMSO for subsequent freezing.

***In vitro* engulfment assay with astrocytes.** Astrocytes were purified from the P4–P6 *Aldh1l1-EGFP* mouse cortex and cultured in serum-free conditions as described previously[15]. Astrocytes at 3–5 days *in vitro* were washed twice with PBS and incubated with appropriate media (see below) containing either tdTomato-expressing or pHrodo-conjugated synaptosomes. For tdTomato-expressing synaptosomes, after incubating with synaptosomes for 4 h, astrocytes were fixed with 4% paraformaldehyde and imaged by confocal microscopy to obtain optical *z*-stacks. Imaris software (BITPLANE) was used to process confocal *z*-stacks to reveal engulfed synaptosomes by astrocytes. For pHrodo-conjugated synaptosomes, live astrocytes were imaged with epifluorescence microscopy after incubating with synaptosomes for 4 h to reveal engulfed pHrodo-conjugated synaptosomes. For testing secreted factors on astrocyte-mediated phagocytosis, pHrodo-conjugated synaptosomes were incubated with purified astrocytes for 24 h in the presence of fresh astrocyte growth media (AGM: 50% neurobasal, 50% DMEM, glutamine, pyruvate, NAC and penicillin-streptomycin, 5 ng ml^{-1} HBEGF), astrocyte-conditioned media (ACM, see below), 5% fetal calf serum (FCS) in AGM or protein S (1 μg ml^{-1}, Abcam) in AGM. To compare phagocytic capacity of astrocytes between wild types and mutants, astrocytes were purified from the P4–P6 wild-type, *Megf10*$^{-/-}$ or *Mertk*$^{-/-}$ cortex and astrocytes at 3–5 days *in vitro* were incubated with pHrodo-conjugated synaptosomes for 24 h in the presence of 5% serum. We used two different methods to quantify the phagocytic capacity: image processing and FACS analysis. For image processing analysis, we took 10 images per well using ×20 objective lens from a random area of the 24-well plates and calculated the phagocytic index by measuring the area of engulfed synaptosomes normalized by the area of astrocytes, using FIJI. Relative engulfment ability was calculated by normalizing the phagocytic index of mutant astrocytes by that of wild-type astrocytes. For FACS analysis, astrocytes were trypsinized, collected by centrifugation, and re-suspended in Dulbecco's PBS (DPBS) containing 0.02% BSA. Live astrocytes were analysed at room temperature by the LSR 2 analyser at the Stanford Shared FACS Facility on the basis of their pHrodo expression intensity. The phagocytic index was calculated by measuring the percentage of the cell population showing strong pHrodo intensity ($>3 \times 10^4$ in pHrodo intensity). Relative engulfment ability was calculated by normalizing the phagocytic index of mutant astrocytes by that of wild-type astrocytes.

***In vitro* engulfment assay with microglia.** To compare phagocytic capacity of microglia between wild types and mutants, enriched microglial cell population was purified from the P4–P6 wild-type, *Megf10*$^{-/-}$ or *Mertk*$^{-/-}$ cortex by the immunopanning method[15] with slight modification. Briefly, cortex from 3–4 mice per genotype were dissected in DPBS and the meninges were removed. Single-cell suspension was produced by dissociating the tissues with papain, and placed in the panning plate coated with rat anti-mouse CD45 (BD Pharmingen). After 20 min, the plate was washed thoroughly to remove any unbound cell, and microglia were collected by trypsinization and centrifugation. Microglia cultured with ACM (see below) at 3–5 days *in vitro* were incubated with pHrodo-conjugated synaptosomes for 24 h in the presence of 5% serum for subsequent FACS analysis. FACS analysis with enriched microglial cells showed two distinct cell populations with low and strong pHrodo intensity. The phagocytic index was calculated by measuring the percentage of the cell population showing strong pHrodo intensity ($>3 \times 10^4$ in pHrodo intensity). Relative engulfment ability was calculated by normalizing the phagocytic index of mutant astrocytes by that of wild-type astrocytes.

Astrocyte-conditioned media. Purified astrocytes were plated in a 10-cm plate and cultured in AGM. After 2 days *in vitro*, old media was replaced with conditioning media (50% neurobasal, 50% DMEM without phenol red, glutamine, pyruvate, NAC and penicillin-streptomycin) and astrocytes were cultured for an additional 7 days to enrich secreted factors from astrocytes. Any dead cell and debris were removed by centrifugation.

***In vivo* engulfment assay.** *Aldh1l1-EGFP* (ref. 2) and *CX3CR1-EGFP* (ref. 22) transgenic lines were used to visualize astrocytes and microglia, respectively, in all *in vivo* engulfment assays, except for the experiments determining the relative contributions of microglia and astrocytes in synapse elimination shown in Extended Data Fig. 6 (in this case, microglia were labelled by IBA1-immunostaining and astrocytes were labelled by *Aldh1l1-EGFP* on the same brain sections). Pups were anaesthetized with isoflurane and 1 μl of cholera toxin-β subunit (CTB) conjugated with Alexa594 and 647 (Invitrogen, 1 mg ml^{-1} in normal saline) were injected into the contralateral and ipsilateral eyes, respectively. After 1–2 days (depending on experiments), mice were perfused with PBS followed by 4% paraformaldehyde and brains were dissected, postfixed overnight for 4 °C and transferred to 30% sucrose for 24 h. The 50 μm floating coronal sections containing dLGN were mounted on slide glasses and used for the analysis. For each animal, two medial-most dLGN were chosen. For each dLGN, two fields (the tip and medial portions of dLGN that contain both contra- and ipsilateral projections) were imaged using Zeiss LSM510 inverted confocal microscopy to obtain 50–70 consecutive optical sections with 0.3 μm interval thickness. FIJI was used to remove outliers (radius 2.0 pixels and threshold 20) from all channels and subtract background from CTB images (rolling bar radius 50 pixels). An image-processing algorithm (Matlab, Mathworks) was used to localize CTB-labelled debris engulfed by glia cells by subtracting CTB-labelled projections outside of glia cells. The phagocytic index was calculated by measuring the total volume of engulfed CTB-labelled debris normalized by the total volume of glia cells in a given *z*-stack. Relative engulfment ability was calculated by normalizing the phagocytic index of experimental groups to control group.

Intraocular injections of epibatidine. P3 *Aldh1l1-EGFP* pups were anaesthetized with isoflurane and 1 μl of epibatidine (Sigma, 1 mM in normal saline) was injected either binocularly or monocularly (for monocular injections, epibatidine was injected into the contralateral eye). Control eyes were also injected with 1 μl of normal saline. Mice received the second intraocular injections of CTB-594 (contralateral) and CTB-647 (ipsilateral) at P4, and the third intraocular injections of epibatidine at P5. The dLGN was collected at P6 for analysis.

Eye segregation analysis. P29 *Megf10* and *Mertk* single/double knockout, and wild-type siblings were anaesthetized with isoflurane and 1 μl of CTB-594 and CTB-488 (Invitrogen, 1 mg ml^{-1} in normal saline) were injected into the left and right eyes, respectively, and the dLGN was harvested at P30. Tissues were prepared and analysed as previously described[36,37].

Array tomography. Tissue preparation, array creation and immunohistochemistry have been described in detail previously[38]. In short, a small piece of tissue (~2 mm high by 1 mm wide by 1 mm deep), in our case P5 dLGN and 1- and 4-month-old somatosensory cortical tissues, was microwave fixed in 4% paraformaldehyde. The fixed tissue was then dehydrated in graded steps of ethanol, and then embedded in LR White resin overnight at 50 °C. The embedded tissue was sectioned on an ultramicrotome at a thickness of 70 nm and placed as a ribbon array directly on gelatin- or carbon-coated glass coverslips.

For image registration and processing, image stacks from AT were imported into FIJI and aligned using both rigid and affine transformations with the Register

Virtual Stacks plugin. The aligned image stacks were further registered across image sessions using FIJI and TrackEM. The aligned and registered image stacks were imported into Matlab and deconvolved using the native implementation of Richardson–Lucy deconvolution with empirical or theoretical PSFs with 10 iterations[20]. Custom functions were written to automate and facilitate this work-flow. Blind deconvolution is also natively implemented in Matlab. Matlab native function (regionprops) was used to calculate the centres of mass of puncta in the image volumes using 26 neighbourhood 3D connected component analyses with an assumed background threshold that is 0.1 of the total dynamic range, which is 6,553.5 for a 16-bit image, and is in line with previous background thresholds used for AT analysis[20]. Custom functions were implemented to facilitate the handling and processing of the data. In Fig. 6 where engulfed synapses by astrocytes were imaged, engulfed excitatory synapses were defined as EYFP (blue) enveloped Bassoon (magenta) and PSD-95 (cyan) that were within 200 nm of each other. Engulfed inhibitory synapses were defined as EYFP (blue) enveloped VGAT (yellow) and Gephyrin (red) that were within 200 nm of each other. The density of engulfed synapses was calculated as the total number of engulfed synapses divided by the volume of EYFP in the image volume.

Serial block face scanning electron microscopy. P5 wild-type animals were perfused transcardially with 0.1 M sodium cacodylate buffer containing 4% PFA and 2% glutaraldehyde. dLGN tissues were dissected out and post-fixed overnight with the same fixative. Subsequent tissue processing and image acquisition were performed by Renovo Neural.

Spontaneous retinal wave recording. Retinal preparations were isolated from P6 mice as previously described[39] and maintained at 34–35 °C. Recordings were analysed offline to isolate the spikes of different cells, as described previously. Briefly, candidate spikes were detected using a threshold on each electrode, and the voltage waveforms on the electrode and nearby electrodes around the time of the spike were extracted. Spikes were projected into the first five principal component dimensions, where an expectation maximization algorithm was used to sort spikes based on a mixture of Gaussians model.

For wave and burst detection, waves and burst occurrences in the spike trains of neurons were detected using modified Poisson surprise algorithms as described previously. Briefly, the time-varying spike count for each neuron was calculated using a 1-s bin. When the probability that a Poisson spike train would generate the spike count calculated for a given bin was $<10^{-5}$, a neuron was considered to be bursting. A wave was considered to have started when >5% of all neurons were bursting. A wave was considered to have ended when <2.5% of all neurons were still bursting. To detect bursts, the spike train of each neuron was analysed. Whenever 3 spikes were found for which the interspike interval (ISI) was less than half the mean ISI of the neuron, the algorithm calculated the initial probability that a Poisson spike train would generate three spikes in a time bin defined by the first and last spike. Spikes were then added one at a time, and the probability was re-calculated. Spikes were added until either the probability increased above the initial value, or the next spike occurred at a time that was greater the mean ISI of the neuron after the preceding spike. If the minimum probability calculated was $<10^{-4}$, then a neuron was considered to have fired a burst.

Wave and burst parameters were calculated as described previously[39]. Briefly, wave speed was calculated by binning each wave into 1-s intervals. The centre of mass of all neurons that were active, weighted by the number of spikes each neuron fired, was calculated for each bin. The distance between centres of mass calculated for successive bins was used to calculate a wave speed. The total wave speed was the average of all wave speeds calculated for successive bins. Wave width was calculated by binning each wave into 1-s intervals and finding all the neurons that burst 1 s before or after a given bin. The width was defined as the maximum distance between neurons bursting before and after the bin. The width of a wave was the average of all these widths calculated for all bins. Burst durations and burst spike rates were computed by averaging all values over the entire recording for each neuron. The time spent spiking above 10 Hz was computed by summing all ISIs <100 ms within a burst. To quantify how high-frequency spiking was distributed among wave bursts and non-wave bursts, we calculated the percentage of the total time spent spiking above 10 Hz that occurred during wave bursts or during non-wave bursts. The correlation index was computed as described previously using a 100-ms coincidence interval.

For wave directionality, the directional bias of individual neurons, as well as each preparation, was calculated as described previously. Briefly, each burst that a neuron fired that occurred during a wave was analysed. Any bursts that occurred 0.5 s before (pre) or after (post) this burst were identified, and the weighted centres of mass of pre- and post-bursts were calculated. Each spike fired by the burst under investigation was assigned the angle between the pre- and post-burst centres of mass (burst spike angle). A neuron was said to have a directional bias if the distribution of all burst spike angles deviated significantly from circular uniformity (Rayleigh test; $P < 0.05$). The directional bias of each neuron was defined as the normalized vector sum of all its burst spike angles. A preparation was said to have a directional bias if the directional bias of all neurons deviated significantly from circular uniformity (Rayleigh test; $P < 0.01$). The directional bias of each preparation was defined as the normalized vector sum of the directional bias of all neurons.

Electrophysiology. Mice aged P15–18 were killed and the brain was rapidly removed and placed into ice-cold choline-based cutting solution containing (in mM): $NaHCO_3$ 26, glucose 25, choline chloride 130, KCl 2.5, NaH_2PO_4 1.25, $MgCl_2$ 7, $CaCl_2$ 0.5. Angled parasagittal brain slices (250 μm) were prepared, using a sapphire blade, according to the method of Turner and Salt, with adaptations[18,23]. This method preserves the optic tract and dLGN, and generally only one slice is obtained per animal. After cutting, slices were incubated at 31 °C for 20 min in choline-based cutting solution followed by 20 min in isotonic saline solution (in mM: NaCl 125, $NaHCO_3$ 25, KCl 2.5, NaH_2PO_4 1.25, glucose 25, $MgCl_2$ 1, $CaCl_2$ 2). Oxygenation was continuously supplied during cutting, recovery and recording. Slices were transferred to a recording chamber and dLGN relay neurons were identified under DIC optics based on their large size and by their number of dendrites (three or more dendrites). Whole-cell voltage-clamp recordings were performed at room temperature in isotonic saline solution containing the $GABA_A$ receptor antagonist GABAzine (10 μM), to block local inhibitory circuits. Patch electrodes with a resistance of 2–2.5 MΩ were filled with an internal solution containing (in mM): CsCl 130, NaCl 4, HEPES 10, EGTA 5, $CaCl_2$ 0.5, MgATP 4, Na_2GTP 0.5, QX-341 5 (to suppress voltage-gated sodium channels), pH adjusted to 7.2 with CsOH. A bipolar simulating electrode, filled with isotonic saline solution, was placed in the optic tract next to the vLGN, in a location that optimized the maximal evoked current. The optic tract was stimulated at intensities of 0–200 μA (duration 0.5 ms), with inter-trial intervals of 30 s. The membrane potential of LGN neurons was clamped at either −70 mV or +40 mV, to measure responses mediated predominantly by AMPA or NMDA receptors, respectively.

Two methods were used to quantify the number of retinal afferents connected to the relay neurons in the dLGN: the fibre fraction method and the step-counting method. For the fibre fraction method, we recorded the single-fibre response by reducing the stimulus intensity until no response could be detected and then increasing the stimulus intensity in small increments (0.5-μA increments) to recruit a single fibre (minimal stimulation). Next, we increased the stimulus intensity to excite the bulk of the optic tract (maximal stimulation) to determine the maximal evoked response. The fibre fraction was calculated by dividing the single fibre current response by the maximal current response, thereby estimating the fraction of the cell's total retinogeniculate input contributed by a single fibre. For the step-counting method, we recorded the synaptic responses of dLGN neurons while varying the stimulus intensity from the minimal stimulation to the maximal stimulation to recruit individual axonal inputs. Separate fibres were interpreted as clusters of postsynaptic current responses recruited by an increase in stimulation. This stimulus–response profile allowed an estimation of the number of afferents to each dLGN neuron. Cells were categorized into three groups; refined (1–2 steps), resolving (3–6 steps) and unrefined (7 or more steps), depending on the number of steps detected in their stimulus-response profile.

Statistical analysis. All statistical analyses were done using GraphPad Prism 6 software.

Most of the data were analysed by one-way ANOVA followed by Dunnett's multiple post-hoc tests for comparing more than three samples, and two-sample un-paired *t*-test for comparing two samples with 95% confidence. Two-sample Kolmogorov–Smirnov test with 95% confidence was used for electrophysiology experiments in Fig. 4c, f.

33. Lu, Q. *et al.* Tyro-3 family receptors are essential regulators of mammalian spermatogenesis. *Nature* **398,** 723–728 (1999).
34. Dunkley, P. R., Jarvie, P. E. & Robinson, P. J. A rapid Percoll gradient procedure for preparation of synaptosomes. *Nature Protocols* **3,** 1718–1728 (2008).
35. Beletskii, A. *et al.* High-throughput phagocytosis assay utilizing a pH-sensitive fluorescent dye. *Biotechniques* **39,** 894–897 (2005).
36. Datwani, A. *et al.* Classical MHCI molecules regulate retinogeniculate refinement and limit ocular dominance plasticity. *Neuron* **64,** 463–470 (2009).
37. Jaubert-Miazza, L. *et al.* Structural and functional composition of the developing retinogeniculate pathway in the mouse. *Vis. Neurosci.* **22,** 661–676 (2005).
38. Micheva, K. D., Busse, B., Weiler, N. C., O'Rourke, N. & Smith, S. J. Single-synapse analysis of a diverse synapse population: proteomic imaging methods and markers. *Neuron* **68,** 639–653 (2010).
39. Stafford, B. K., Sher, A., Litke, A. M. & Feldheim, D. A. Spatial-temporal patterns of retinal waves underlying activity-dependent refinement of retinofugal projections. *Neuron* **64,** 200–212 (2009).

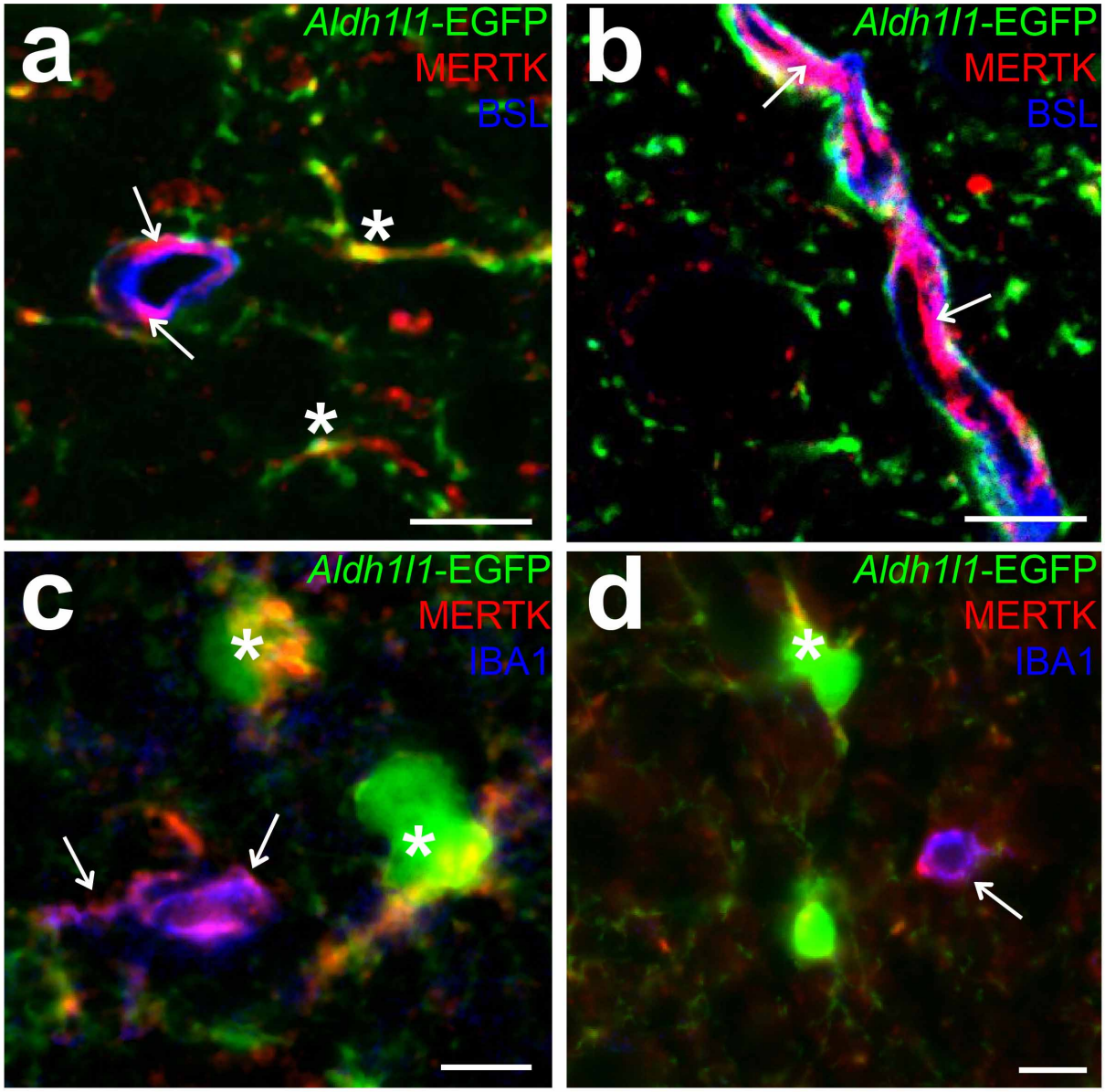

Extended Data Figure 1 | MERTK protein is localized to multiple cell types. **a**, **b**, Confocal P5 dLGN images showing MERTK (red) protein expression in endothelial cells (arrows) stained with BSL (blue) as well as in astrocytic processes (asterisks) labelled by *Aldh1l1-EGFP* (green). **c**, **d**, Confocal P5 dLGN images showing MERTK (red) protein expression in microglia (arrows) stained with IBA1 (blue) as well as in astrocytes (asterisks) labelled by *Aldh1l1-EGFP* (green). Scale bar: 10 μm.

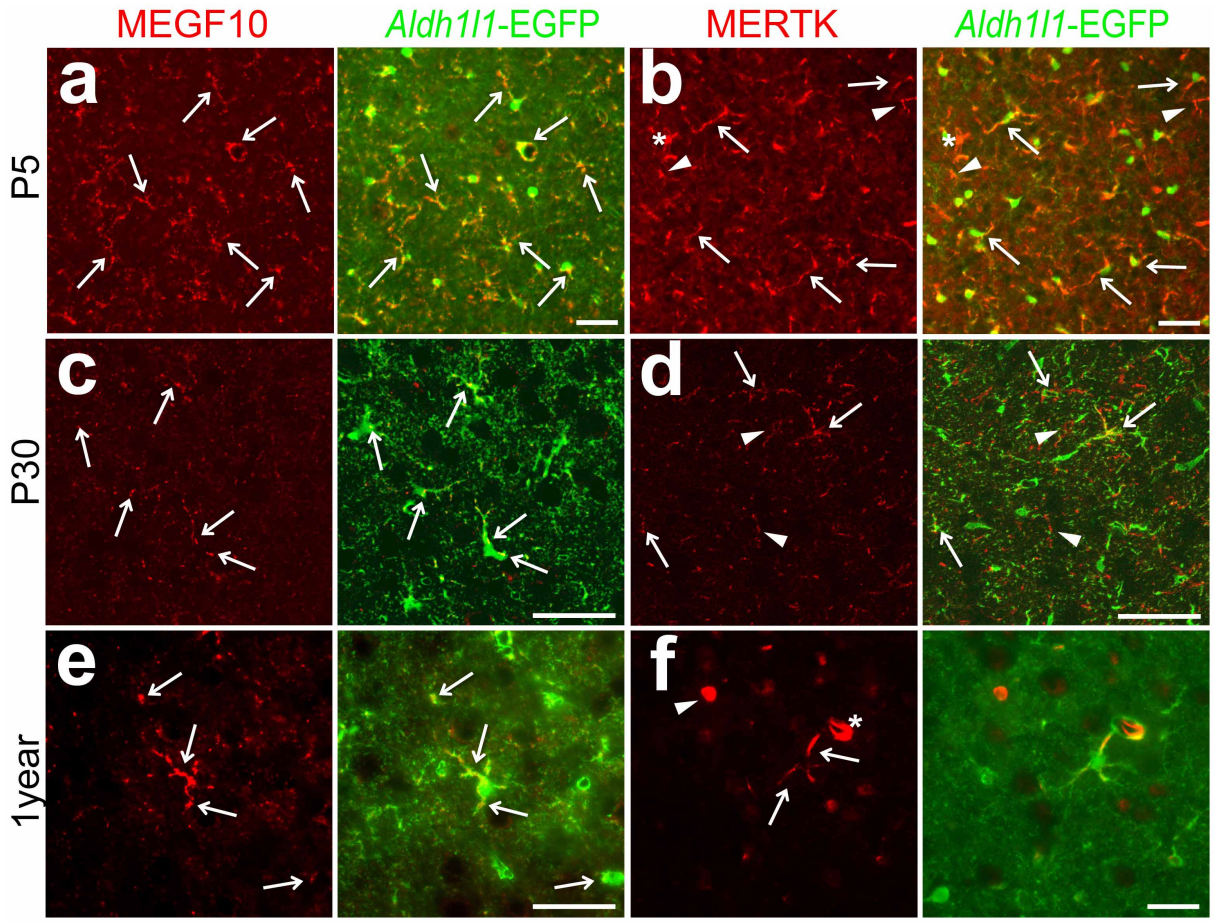

Extended Data Figure 2 | MEGF10 and MERTK are continuously localized to cortical astrocytes throughout life. **a**–**f**, MEGF10 (red; **a**, **c**, **e**) and MERTK (red; **b**, **d**, **f**) are localized to cortical astrocytes (arrows) labelled by *Aldh1l1-EGFP* (green) in the P5 (**a**, **b**), P30 (**c**, **d**) and 1-year-old (**e**, **f**) mouse cortex. Whereas MEGF10 is specifically localized to astrocytes, MERTK is also localized to microglia (arrowheads) as well as endothelial cells (asterisks). Scale bar: 20 μm.

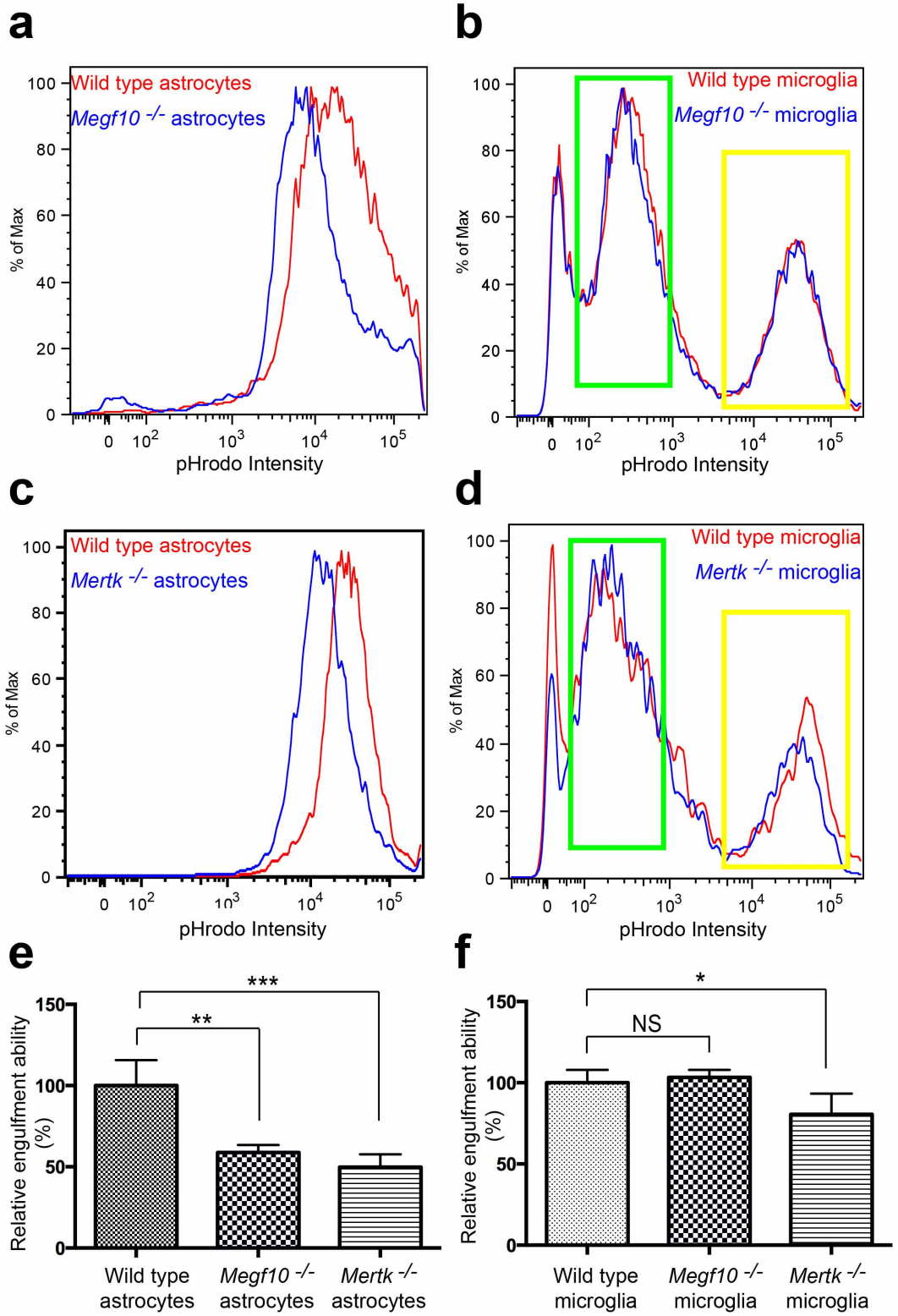

Extended Data Figure 3 | Phagocytic capacity of *Megf10*$^{-/-}$ or *Mertk*$^{-/-}$ astrocytes and microglia measured by FACS. a–d, FACS profiles of astrocytes (**a**, **c**) and enriched microglia population (**b**, **d**) for pHrodo intensity after incubating with pHrodo-conjugated synaptosomes for 24 h in the presence of 5% serum. *Megf10*$^{-/-}$ (**a**) and *Mertk*$^{-/-}$ (**c**) astrocytes (blue lines) show clear leftward shifts in pHrodo intensity compared to wild-type astrocytes (red lines). *Megf10*$^{-/-}$ microglia (**b**, blue line) do not show any difference in the FACS profile compared to wild-type microglia (red lines in **b**). *Mertk*$^{-/-}$ microglia (**d**, blue line) exhibit a slight leftward shift in the FACS profile showing strong pHrodo intensity (yellow rectangle) whereas there is no difference in low pHrodo intensity (green rectangle) compared to wild-type microglia. **e**, *Megf10*$^{-/-}$ and *Mertk*$^{-/-}$ astrocytes show a 42% and 51% reduction in the relative engulfment ability, respectively, compared to wild-type astrocytes. **f**, *Mertk*$^{-/-}$ microglia show a 25% reduction in the relative engulfment ability compared to wild-type microglia. The relative engulfment ability was calculated by comparing the percentage of the cell population expressing strong pHrodo intensity ($>3 \times 10^4$). Representative data from three independent experiments are shown. $^*P < 0.05$, $^{**}P < 0.01$, $^{***}P < 0.001$, one-way ANOVA. NS, not significant. Error bars indicate s.e.m.

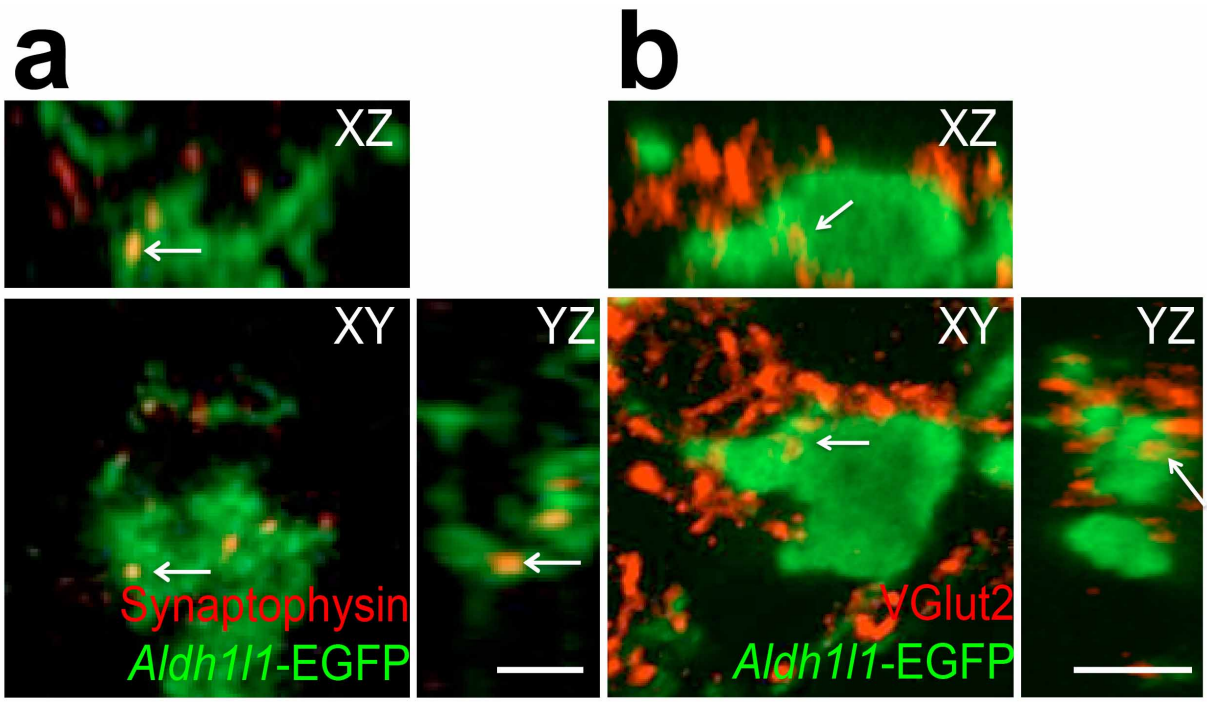

Extended Data Figure 4 | Astrocytes in the developing dLGN engulf presynaptic material. **a**, **b**, Optical sections of the P5 dLGN using structured illumination (**a**) and confocal (**b**) microscopy through *xy*, *xz* and *yz* axes show that synaptophysin- (**a**, arrows) and VGlut2- (**b**, arrows) positive presynaptic material are engulfed by EGFP-expressing astrocytes (green). Scale bar: 1 μm (**a**); 5 μm (**b**).

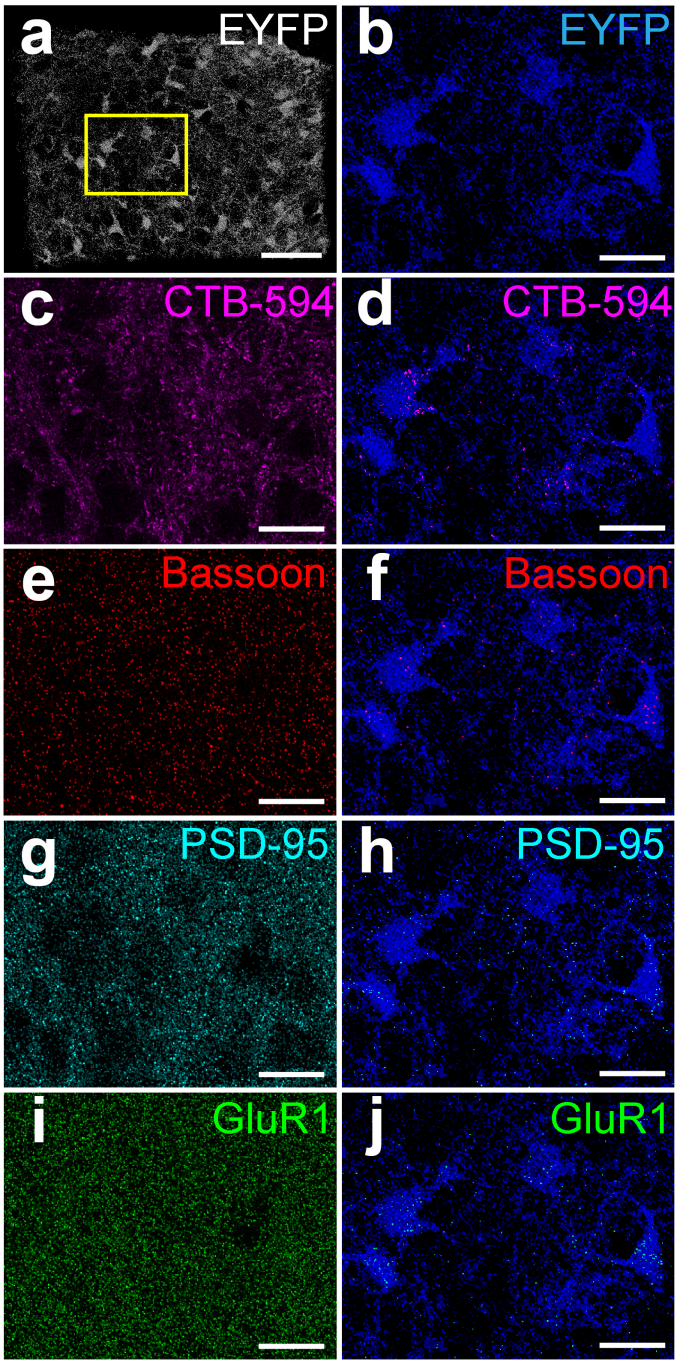

Extended Data Figure 5 | Astrocytes in the developing dLGN engulf pre- and postsynaptic material, revealed by array tomography (AT). **a**, 3D-max projection AT images showing EYFP (grey)-labelled P5 dLGN astrocytes (total volume = 155 μm by 125 μm by 2.8 μm). **b**, Close-up view of EYFP (blue)-labelled dLGN astrocytes. **c**, **d**, Close-up view of 3D-max projection AT images showing CTB-594 labelled projections (magenta) before (**c**) and after (**d**) image processing, revealing engulfed CTB-labelled debris by astrocytes (blue). **e**, **f**, Close-up view of 3D-max projection AT images showing Bassoon (red) before (**e**) and after (**f**) image processing, revealing engulfed Bassoon-positive synaptic material by astrocytes (blue). **g**, **h**, Close-up view of 3D-max projection AT images showing PSD-95 (cyan) before (**g**) and after (**h**) image processing, revealing engulfed PSD-95-positive synaptic material by astrocytes (blue). **i**, **j**, Close-up view of 3D-max projection AT images showing GluR1 (green) before (**i**) and after (**j**) image processing, revealing engulfed GluR1-positive synaptic material by astrocytes (blue). Scale bar: 50 μm (**a**); 20 μm (**b**–**j**).

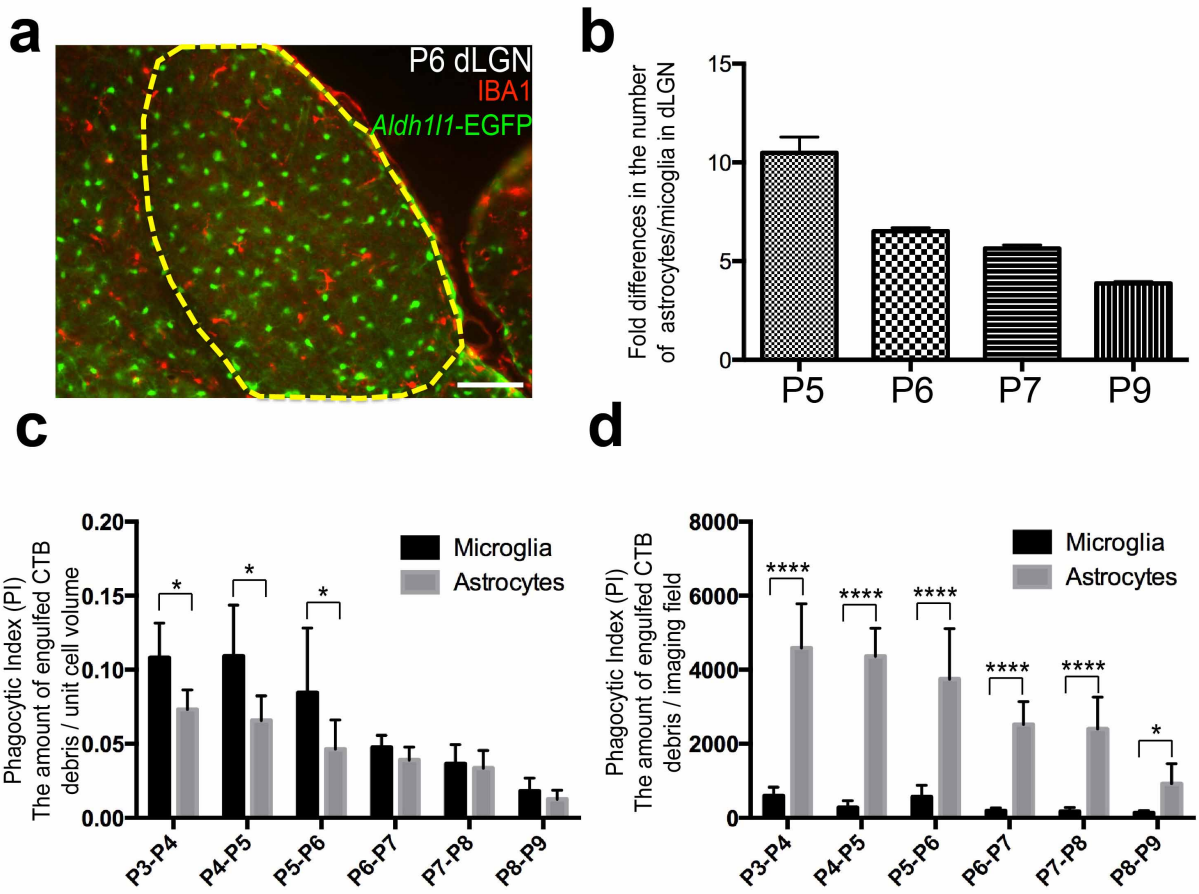

Extended Data Figure 6 | Astrocytes clear neural debris more robustly than microglia in the developing dLGN. **a**, Representative image of P6 dLGN (yellow dotted line) showing astrocytes labelled by *Aldh1l1-EGFP* (green) and microglia labelled by IBA1 staining (red). **b**, The number of astrocytes in dLGN is much greater than microglia at P5 (10-fold), P6 (7-fold), P7 (6-fold) and P9 (4-fold). **c**, The phagocytic index measured by the total amount of CTB debris per unit cell volume showed that during P3–P6, microglia engulfed more CTB-labelled debris than astrocytes per unit cell volume, whereas astrocytes and microglia cleared about the same amount of debris per unit cell volume after P6. $n = 5$ per group. **d**, The phagocytic index measured by the total amount of CTB debris per imaging field showed that astrocytes clear a significantly greater amount of CTB debris than microglia during P3–P9. $n = 5$ per group. $^{*}P < 0.05$, $^{***}P < 0.001$, *t*-test. Error bars indicate s.e.m.

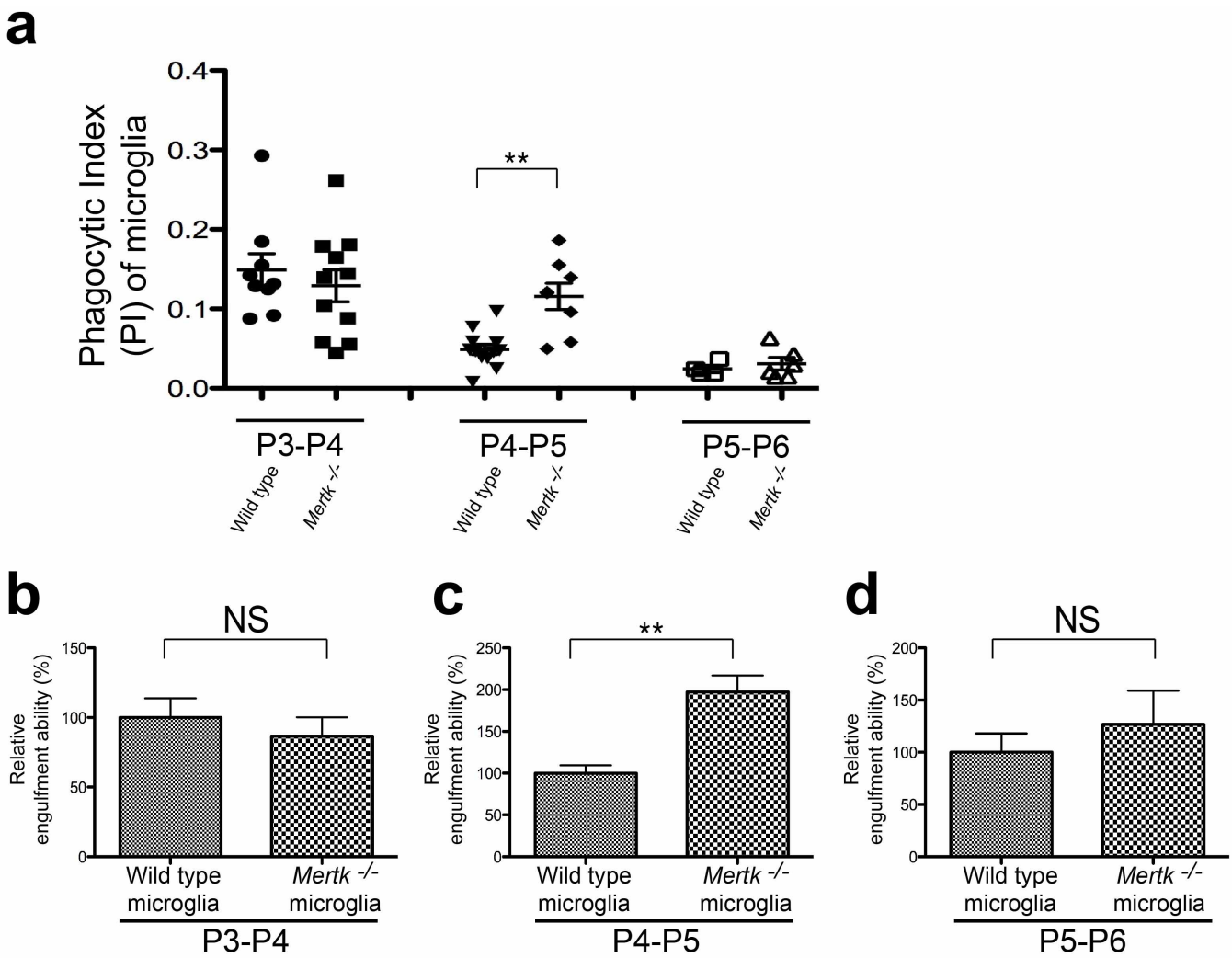

Extended Data Figure 7 | MERTK is dispensable for the microglia-mediated phagocytosis in developing dLGN. **a**, Comparing the phagocytic index of microglia in dLGN during P3–P6 between wild-type and *Mertk*$^{-/-}$ mice. Microglia showed a gradual decrease in the phagocytic index measured from P3 to P6. **b**–**d**, Relative engulfment ability between wild-type and *Mertk*$^{-/-}$ microglia during P3–P4 (**b**), P4–P5 (**c**) and P5–P6 (**d**). *Mertk*$^{-/-}$ microglia showed a transient increase in the phagocytic index during P4–P5. However, the phagocytic index of microglia during P3–P4 and P5–P6 was comparable between wild-type and *Mertk*$^{-/-}$ mice. $n = 4$ per group. $^{**}P < 0.01$, *t*-test. NS, not significant. Error bars indicate s.e.m.

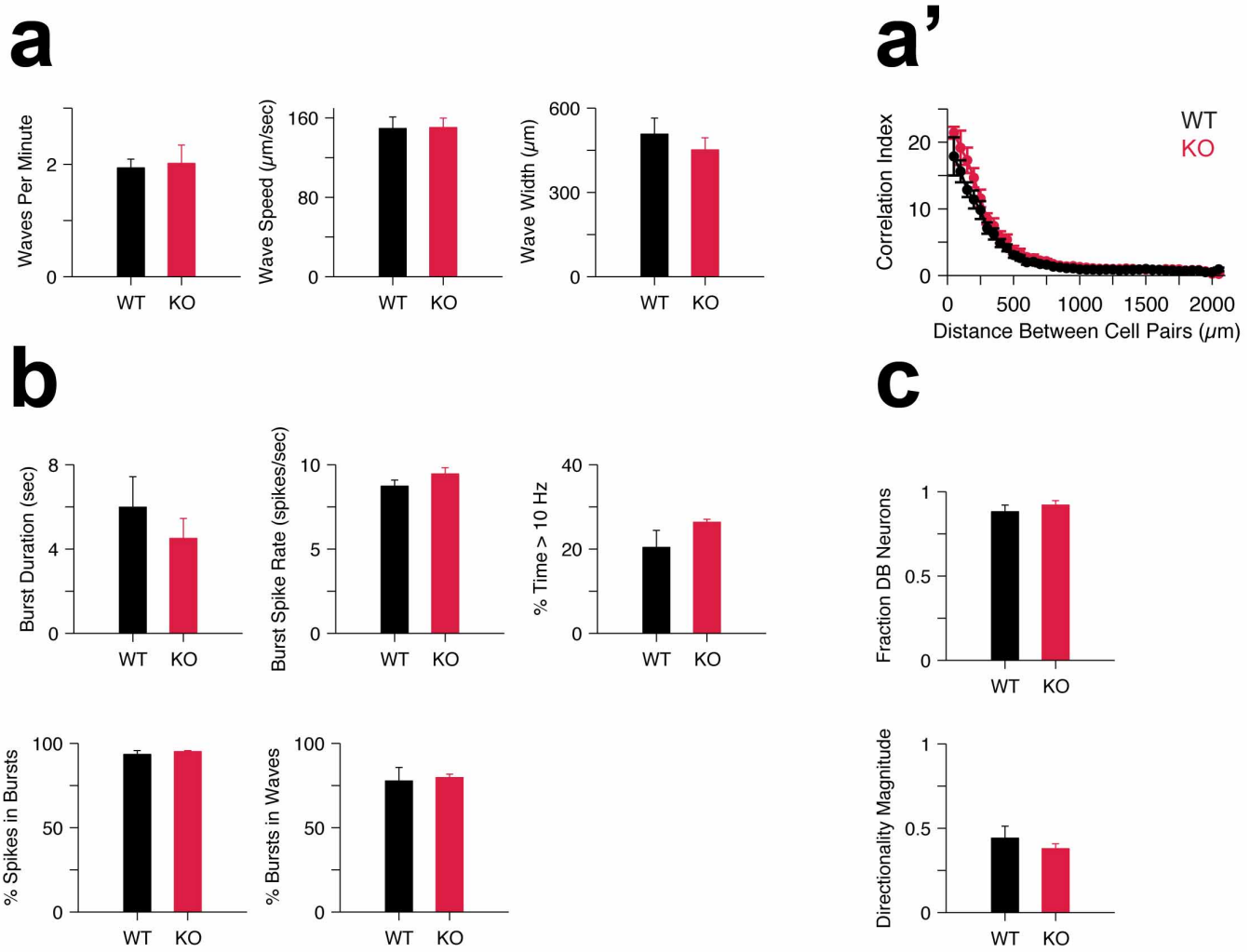

Extended Data Figure 8 | Spontaneous retinal wave is intact in *Megf10*$^{-/-}$; *Mertk*$^{-/-}$ mice. **a**, Waves occur with the same frequency (left), propagate at the same speed (middle), and are the same size (right) in *Megf10*$^{-/-}$; *Mertk*$^{-/-}$ retinas. **a′**, Correlation index (CI), computed for spike trains from pairs of neurons and plotted as a function of the distance between electrodes on which the neurons were recorded, shows that CI decreases as a function of distance in both wild-type and *Megf10*$^{-/-}$; *Mertk*$^{-/-}$ retinas. Plots summarize data from multiple wild-type (black; $n = 5$) and *Megf10*$^{-/-}$; *Mertk*$^{-/-}$ (red; $n = 5$) preparations. **b**, Bursts fired by ganglion cells show no difference in duration (top left), mean spike rate (top middle), or the amount of time spent firing at high frequencies (top right) in *Megf10*$^{-/-}$; *Mertk*$^{-/-}$ retinas. The per cent of all spikes that are incorporated into bursts (bottom left), and the per cent of all bursts that occur during waves (bottom right), are also unchanged in *Megf10*$^{-/-}$; *Mertk*$^{-/-}$ retinas. Plots summarize data from multiple wild-type (black; $n = 5$) and *Megf10*$^{-/-}$; *Mertk*$^{-/-}$ (red; $n = 5$) preparations. **c**, Quantification of directionality parameters shows that the same fraction of ganglion cells demonstrates a directional bias in *Megf10*$^{-/-}$; *Mertk*$^{-/-}$ retinas (top). In addition, the magnitude of the directional bias of all neurons in a preparation (bottom) is unchanged in *Megf10*$^{-/-}$; *Mertk*$^{-/-}$ retinas. Plots summarize data from multiple wild-type (black; $n = 5$) and *Megf10*$^{-/-}$; *Mertk*$^{-/-}$ (red; $n = 5$) preparations. *t*-test.

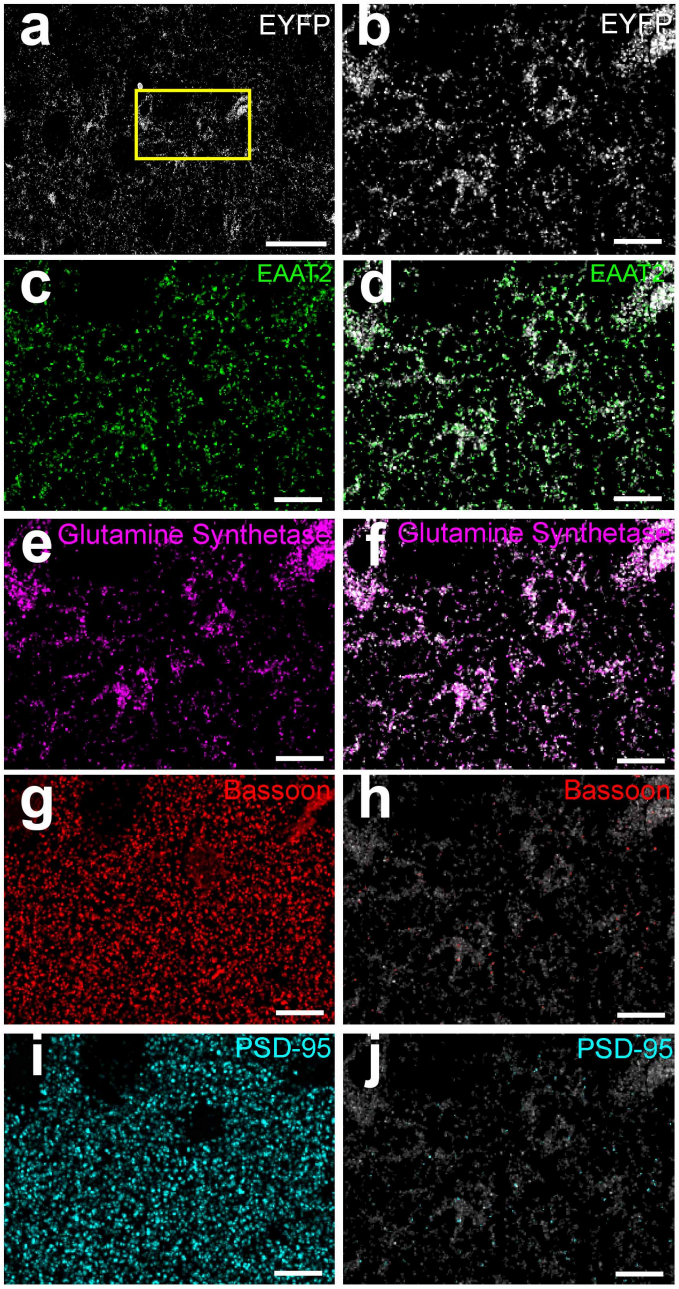

Extended Data Figure 9 | Analysis of astrocytic and synaptic protein localization by array tomography (AT) in the adult cortex with EYFP-expressing astrocytes. **a**, 3D-max projection AT images showing EYFP (grey)-labelled astrocytes from the 4-month-old somatosensory cortex (total volume = 155 µm by 125 µm by 2.8 µm). **b**, Close-up view of EYFP (grey)-labelled cortical astrocytes. **c**–**f**, Close-up views of 3D-max projection AT images showing EAA2 (**c**, **d**; green) and glutamine synthetase (**e**, **f**; magenta) staining reveal specific expression of EYFP in astrocytes (**d**, **f**; grey). **g**, **h**, Close-up view of 3D-max projection AT images showing Bassoon (red) before (**g**) and after (**h**) image processing, revealing engulfed Bassoon-positive synaptic material by astrocytes (grey). **i**, **j**, Close-up view of 3D-max projection AT images showing PSD-95 (cyan) before (**i**) and after (**j**) image processing, revealing engulfed PSD-95-positive synaptic material by astrocytes (grey). Scale bar: 50 µm (**a**); 20 µm (**b**–**j**).